alloys

MDPI

Article

Evolution of Microstructural Features and Electrochemical Corrosion Assessment of Ga-Doped CoCrFeNi High-Entropy Alloys: A Comparative Study

Emmanuel Georgatis, Anthoula Poulia, Stavros Kiape, Aikaterini Lefa, Christina Prosili, Margarita Ziavra, Theodore E. Matikas and Alexander E. Karantzalis *

Department of Materials Science and Engineering, University of Ioannina, 45100 Ioannina, Greece; mgeorgat@uoi.gr (E.G.); apoulia@uoi.gr (A.P.); s.kiape@uoi.gr (S.K.); katerinalefa888@gmail.com (A.L.); christinaprosili@gmail.com (C.P.); ziavramargarita@gmail.com (M.Z.); matikas@uoi.gr (T.E.M.)
* Correspondence: akarantz@uoi.gr

Abstract

This study investigates the microstructural evolution of the CoCrFeNi system after incorporating Gallium (Ga) at varying concentrations (0, 15, and 20 at.%). The systems were synthesized by Vacuum Arc Melting (VAM) and characterized through X-ray Diffraction diffraction (XRD) and Scanning Electron Microscopy (SEM/EDS). Findings showed that the CoCrFeNi medium medium-entropy alloy stabilizes in a single-phase Face-Centered Cubic (FCC) structure. Upon the addition of 15 at.% Ga a dendritic morphology with a transition towards a duplex FCC + BCC microstructure was induced, a trend which was further solified in the equiatomic FeCoNiCrGa system. In this case the proportion of the Ga-rich BCC phase was increased from 18–22% to 31–34% for the Ga15 and Ga20 systems respectively. A combined approach of Electrochemical Frequency Modulation (EFM), Cyclic Potentiodynamic Polarization (CPP), and Electrochemical Impedance Spectroscopy (EIS) was selected for studying the electrochemical corrosion behavior of the produced systems. EFM results indicated a progressive deterioration of corrosion resistance when increasing Ga concentration (Icorr: 4.142, 5.619 and 10.01 $\mu A/cm^2$, and Rp: 12,035, 10,736 and 7254 Ω for the Ga0, Ga15 and Ga20 alloys respectively). Surface inhomogeneity, rapid passivation, and diffusion-controlled processes caused deviations from the ideal causality factors' values. CPP measurements revealed increasing corrosion current densities with Ga addition within the Tafel region (2.81×10^{-7}, 3.72×10^{-7} and $5.11 \times 10^{-7} A/cm^2$ for the Ga0, Ga15 and Ga20 alloys respectively). All alloys showed positive hysteresis loops and an absence of repassivation, indicating susceptibility to pitting corrosion. Nevertheless, detailed analysis of the forward polarization region highlighted a more complex aspect. Reverse polarization scans confirmed stable pit growth in all alloys, with the absence of a repassivation tendency. EIS tests, performed after the completion of CPP measurements, further clarified the corrosion mechanisms. Equivalent circuit modeling revealed that although Ga-containing alloys exhibited relatively improved film characteristics in the forward polarization stage, the charge transfer resistance (Rct) was highest for the CoCrFeNi alloy, followed by Ga15 and Ga20 (22,620, 11,380, 10,060 Ω respectively). The overall impedance ranking (Ga0 > Ga15 > Ga20, i.e., 27,139 > 20,279.5 > 16,341 ohms respectively) showed that, despite microstructural and entropic effects enhancing certain passivation aspects, the reduced Cr content highly impacted long-term corrosion resistance. This holistic electrochemical approach showcases the complex interactions between compositional alterations, phase structure, grain refinement, passive film chemistry, and diffusion trends in establishing the corrosion performance of Ga-modified CoCrFeNi HEAs.

Check for updates

Academic Editor: Konstantinos Georgarakis

Received: 19 March 2026
Revised: 22 May 2026
Accepted: 29 May 2026
Published: 30 May 2026

Copyright: © 2026 by the authors. Licensee MDPI, Basel, Switzerland. This article is an open access article distributed under the terms and conditions of the Creative Commons Attribution (CC BY) license.

Keywords: high-entropy alloys; CoCrFeNiGa; phase formation criteria; microstructural evolution; electrochemical properties; electrochemical frequency modulation; cyclic potentiodynamic polarization; electrochemical impedance spectroscopy

1. Introduction

High-entropy alloys (HEAs) represent a paradigm shift in metallurgy, moving away from single element-based solvent systems toward concentrated solid solutions containing five or more principal elements in near-equiatomic proportions [1,2]. The stability of these systems is governed by the high configurational entropy of mixing, which serves to minimize the Gibbs free energy, thereby suppressing the formation of brittle intermetallic phases in favor of simple FCC, BCC, or HCP solid solutions [3]. Among the most studied systems is the CoCrFeNi medium-entropy alloy, renowned for its exceptional ductility and corrosion resistance, attributed to its stable FCC lattice [4]. However, the modest yield strength of the base FCC matrix often necessitates the introduction of alloying elements with larger atomic radii or different electronic configurations to induce lattice distortion or phase transformations [5].

Gallium, a post-transition metal, presents an intriguing candidate for alloying due to its unique electronic state and its tendency to influence the Valence Electron Concentration (VEC) [6]. As Ga is introduced into the CoCrFeNi matrix, the system transitions from a medium-entropy alloy to a high-entropy alloy, significantly altering the thermodynamic landscape.

Limited work on Ga addition in HEAs has been reported in the literature. Indicatively, Liu et al. [7] studied the influence of different Ga additions in an FeCoCrNi medium-entropy basic core in order to achieve an appropriate new high-entropy alloy composition that possesses the optimum balance between mechanical properties and damping capacity. Vida et al. [8] also introduced Ga additions in an FeCoCrNi core, in an effort to examine the possible microstructural phase alterations at different heat treatments. In a similar approach, Molnar et al. [9] examined the effect of different cooling rates on the stability/alteration of the potential to form phases. It is worth mentioning that in both these works [8,9] the driving force was the ability of Ga to turn the FeCoCrNi system from a paramagnetic alloy to a new ferromagnetic system by the formation of BCC phases. Luo and Zhou [10] revealed a new field for the use of Ga in high-entropy alloy applications. They presented the use of Ga in a series of low-temperature liquid phase sintering processes, where, depending on the host primary medium-entropy alloy core, they reported exceptional results as potential Ga-based FCC electrocatalytic systems of superior oxygen evolution, as Ga-based BCC refractory HEAs for aerospace applications and as Ga-based FCC soft magnetic alloys for electronic devices and electro-packaging applications. Additionally, Wang et al. [11] reported the beneficial effect of Ga addition in a Ti-Zr-Nb alloy core, producing new medium-entropy alloy systems that showed exceptional behavior in diminishing bacterial colonization and promoting osteogenesis. Similar behavior of Ga for potential biomedical applications was reported by Zhu et al. [12] while developing Ti-Zr-Nb-Ta high-entropy alloys with various Ga additions.

In addition to the microstructural transformations, the electrochemical response of CoCrFeNi-based HEAs is a critical factor for their structural integrity in saline environments. Conventional methods such as Linear Polarization Resistance (LPR) and Tafel extrapolation are standard for determining corrosion rates [13]. However, Tafel extrapolation requires large potential polarizations that can irreversibly disturb the electrode surface, making it less ideal for instantaneous or repeated measurements. To overcome these limitations,

this study employs Electrochemical Frequency Modulation (EFM), a relatively recent non-destructive technique that allows for the simultaneous determination of corrosion current density (i_{corr}) and Tafel slopes without prior knowledge of these parameters [14]. While EFM has been successfully applied to study corrosion in acid media and inhibited systems, there is currently no systematic reporting in the literature regarding its application to the complex, multi-component surfaces of HEAs.

The instantaneous insights from EFM can be further validated using Cyclic Potentiodynamic Polarization (CPP) and Electrochemical Impedance Spectroscopy (EIS). CPP is instrumental in identifying the transition from the Tafel region to a stable passive state, as well as susceptibility to pitting indicated by positive hysteresis loops [15]. Complementarily, EIS allows for the modeling of the electrochemical interface using equivalent electric circuits [16]. In this work, sophisticated models incorporating Constant Phase Elements (CPEs) are used to account for surface inhomogeneities, while Warburg impedance elements are introduced for Ga-doped systems to address observed diffusion-controlled processes.

Concerning strictly the effect of Ga on the corrosion resistance of high-entropy alloys, limited research effort has been reported in the literature. Despite these limitations, the work of Sanchez-Carrillo et al. [17] must be mentioned; they systematically studied the electrochemical response of a Co38.3Ni32.1Ga29.6 alloy by means of polarization curves and reported that different corrosion responses depended on different corrosive environments. Additionally, Gebert et al. [18] examined the passivity of polycrystalline NiMnGa alloys and revealed the importance of the alloys' microstructure (martensitic and/or austenitic) in altering the corrosion response.

This study systematically compares the microstructural fingerprints of the three systems—CoCrFeNi (Ga0), $(FeCoNiCr)_{85}Ga_{15}$ (Ga15), and FeCoNiCrGa (Ga20)—to elucidate the mechanisms of phase selection and the accuracy of current predictive models in Gallium-containing 3d-transition metal HEAs. It also underscores Gallium's role as a potent BCC stabilizer in 3d-transition metal HEAs, thus providing a framework for future optimization of these advanced materials. The authors decided to select these compositions as: (a) a classic approach, when developing new HEAs, is to firstly try the iso-atomic elemental participation. Under this frame, the 20Ga alloy was selected as a logical step to move from the medium-entropy FeCoNiCr system to the high-entropy level by the addition of Ga equiatomic to the rest of the elements' addition. (b) Since the present effort is a part of an extended experimental work concerning the effect of Ga at different proportions, the authors decided, in this instance, to indicatively include another Ga-containing system of lower concentration simply for comparison reasons. The work will be enriched and expanded for both higher-than-20%-Ga and other lower-than-15%-Ga concentrations.

Last but not least, the scope of the present effort is: (a) to examine the effect of Ga addition on altering the microstructure of the basic FeCoCrNi alloy; (b) to provide by combining diverse electrochemical techniques—for the first time in the relevant literature—a comprehensive framework for understanding how Gallium-induced phase transitions affect the corrosion resistance of 3d-transition metal HEAs.

2. Materials and Methods

2.1. Synthesis and Structural Characterization

All three alloy systems were synthesized by utilizing the Vacuum Arc Melting (VAM) technique. High-purity elemental flakes and granules (typically >99.9%) were weighed to precise stoichiometric ratios using analytical balances (Mettler Toledo, AB135-S/FACT, Greifensee, Switzerland). The melting process was conducted in a water-cooled copper plate under a high-purity Argon atmosphere to prevent oxidation, with the vacuum cham-

ber evacuated to at least 10^{-2} mbar prior to purging. To ensure chemical homogeneity, each ingot was flipped and re-melted at least five times.

Characterization of the crystal structure was performed through X-ray diffraction (XRD: D8 Advance; Bruker, Billerica, MA, USA). The radiation source was CuKa, the diffraction angle range (2θ) was 10–120° and the scanning rate was 0.01°/s. Microstructural analysis and chemical mapping were conducted using Scanning Electron Microscopy (SEM) (JEOL 6510 LV, JEOL Ltd., Akishima, Tokyo, Japan) equipped with Energy Dispersive X-ray Spectroscopy (EDS) (Oxford Instruments Ltd., Abingdon, Oxfordshire, UK).

In order to gain information on the relative fraction of the involved phases, image analysis was performed using Image J software (Image J 1.54 g, Wayne Rasband and Contributors, National Institutes of Health, USA, http://imagej.org, java 1.8.0_345).

In order to ascertain a grain size estimate for the Ga15 and Ga20 systems, the linear intersection method was used in different SEM images. At least ten different lines of known length were drawn for each system and the number of grain boundary intersection points was measured. By dividing the line length by the corresponding intersection points an average grain size is obtained.

2.2. Electrochemical Frequency Modulation (EFM) Testing: Theoretical Considerations and Data Analysis

A diverse range of electrochemical techniques is available for quantifying corrosion rates, most notably the Linear Polarization Resistance (LPR) method [19–22], Tafel extrapolation [23,24], and Electrochemical Impedance Spectroscopy (EIS). These methodologies are particularly effective for determining instantaneous corrosion rates, provided that the anodic and cathodic Tafel slopes (b_a and b_c, respectively) are accurately characterized. While the Tafel extrapolation method remains a fundamental tool for deriving both corrosion rates and kinetic parameters, it is generally considered unsuitable for real-time, instantaneous monitoring. This limitation arises because the technique necessitates substantial potential polarization over a relatively wide range, analogous to the extensive polarization required when analyzing copper in sulfate solutions to determine corrosion current. Consequently, this process is not only time-consuming but also risks irreversibly altering the electrode surface morphology and the electrochemical environment, potentially compromising the integrity of subsequent measurements.

Non-linear electrochemical perturbations, typically induced by the application of one or more sinusoidal signals, generate responses across a broader frequency spectrum than that of the input signal due to the inherent non-linearity of the corrosion process. This phenomenon facilitates the acquisition of current responses at zero, harmonic, and intermodulation frequencies. Specifically, the Faraday rectification technique enables the measurement of the direct current (DC) at the "zero" frequency; when at least one Tafel parameter has been previously characterized, this approach can be effectively employed to quantify the corrosion rate.

Furthermore, comprehensive analysis of harmonic frequencies allows for the simultaneous determination of the corrosion rate and both anodic and cathodic Tafel parameters [19–21]. Such harmonic analysis has been extensively utilized to evaluate corrosion kinetics in acidic media, both in the presence and absence of inhibitors [22–24]. A specialized derivative of this methodology is Harmonic Impedance Spectroscopy (HIS), wherein harmonic current components are converted into harmonic impedances. HIS has proven particularly effective for assessing the corrosion rates of polarized systems [24–26], offering a sophisticated means of characterizing complex electrochemical interfaces.

Notably, despite its analytical potential, the application of Electrochemical Frequency Modulation (EFM) in characterizing electrochemical corrosion phenomena has received surprisingly limited attention. To the best of the authors' knowledge, there is currently no

systematic EFM-based study addressing the electrochemical corrosion response of high-entropy alloys (HEAs). In an EFM experiment, the corrosion system is subjected to a potential perturbation consisting of two superimposed sine waves of different frequencies. This non-linear perturbation generates an alternating current (AC) response that comprises components not only at the harmonics of the two fundamental frequencies (ω1, 2ω1, 3ω1,..., ω2, 2ω2, 3ω2...) but also at various intermodulation frequencies (ω1 ± ω2, 2ω1 ± ω2, 2ω2 ± ω1,...). By analyzing these specific current components, the kinetic parameters of the corrosion process can be determined directly, offering a sophisticated alternative to traditional steady-state techniques.

In practice, the Electrochemical Frequency Modulation (EFM) technique quantifies the current density response at the harmonics of the fundamental frequencies ($i_{\omega1}$, $i_{2\omega1}$, $i_{3\omega1}$,..., $i_{\omega2}$, $i_{2\omega2}$, $i_{3\omega2}$,...), as well as at the intermodulation frequencies ($i_{\omega1 \pm \omega2}$, $i_{2\omega1 \pm \omega2}$, $i_{2\omega2 \pm \omega1}$,...). These specific current density components facilitate the direct calculation of critical kinetic parameters, namely the anodic and cathodic Tafel slopes (b_a and b_c) and the corrosion current density (i_{corr}). The fundamental governing equations for b_a, b_c, and i_{corr} are provided below for the reader's convenience:

$$i_{corr} = \frac{{i_{\omega1,\omega2}}^2}{2\sqrt{8i_{\omega1.\omega2}i_{2\omega2\pm\omega1} - {3_{\omega2\pm\omega1}}^2}} \quad (1)$$

$$b_a = \frac{i_{\omega1.\omega2}U_0}{i_{\omega1\pm\omega2} + \sqrt{8i_{\omega1,\omega2}i_{2\omega2\pm\omega1} - 3{i_{\omega2\pm\omega1}}^2}} \quad (2)$$

$$b_c = \frac{i_{\omega1.\omega2}U_0}{-i_{\omega1\pm\omega2} + \sqrt{8i_{\omega1,\omega2}i_{2\omega2\pm\omega1} - 3{i_{\omega2\pm\omega1}}^2}} \quad (3)$$

In Equations (2) and (3), U_0 is the amplitude of the excitation potential wave.

In the present study, a potential excitation signal with an amplitude of 20 mV was employed for both fundamental frequencies, which were specifically set at 0.2 Hz and 0.7 Hz. Although Bosch et al. [19], Kus et al. [27], and Obot et al. [14] have noted the absence of definitive guidelines for the "optimal" selection of these frequencies, several fundamental criteria must be satisfied. Specifically: (a) the chosen frequencies must ensure that the resulting harmonic and intermodulation components do not overlap or interfere with one another; (b) to minimize the influence of the electrochemical double-layer capacitance, the frequencies should be as low as possible; and (c) conversely, the frequencies must be sufficiently high to ensure a practical and efficient experimental duration. Based on these considerations, the authors maintain that the selected frequency pair of 0.2 and 0.7 Hz effectively satisfies these conflicting requirements, providing a reliable basis for the EFM analysis.

A significant advantage of the EFM technique is its capacity for internal data validation through the application of causality factors. These factors are derived from the theoretical relationships between the current response magnitudes at harmonic frequencies and those at intermodulation frequencies [14]. The most widely utilized indicators are the causality factors CF-2 and CF-3, which possess ideal theoretical values of 2.0 and 3.0, respectively. Deviations from these integers serve as a diagnostic tool to identify potential experimental artifacts, such as excessive background noise or non-causal system behavior. The governing equations employed for their calculation are defined as follows:

$$Causality\ factor\ 2(CF-2) = \frac{i_{\omega1\pm\omega2}}{i_{2\omega1}} = 2 \quad (4)$$

$$Causality\ factor\ 3(CF-3) = \frac{i_{2\omega 1 \pm \omega 2}}{i_{3\omega 1}} = 3 \quad (5)$$

Analogous to the determination of b_a, b_c and i_{corr}, the causality factors CF-2 and CF-3 are calculated directly by the Gamry electrochemical analysis software utilized in this study. The degree of deviation between these calculated values and their theoretical ideals (2.0 and 3.0, respectively) serves as a sensitive indicator of experimental noise; smaller deviations reflect a diminished influence of stochastic interference. Conversely, the attainment of values precisely equal to 2.0 and 3.0 signifies a strictly causal relationship between the input potential perturbations and the resulting current response, confirming the validity of the non-linear electrochemical model [14,27]. Once the parameters b_a, b_c and i_{corr} are calculated, by using the Stern–Geary expression [28], Equation (6), the polarization resistance (R_p) for each system can be calculated:

$$i_{corr} = \frac{b_a b_c}{2.303(b_a + b_c)R_p} \quad (6)$$

It is important at this point to further mention the significance and the novel character of the EFM technique when trying to ascertain the electrochemical behavior of an alloy system. The EFM technique is: (a) a non-destructive technique that provides important electrochemical parameter data (such as i_{corr} and Tafel slopes) which directly give the corrosion response; (b) the technique is very fast and the data is collected in a short period of time (a few minutes), giving the scholar a high degree of comfort and flexibility; (c) due to the scientific frame of the method, crucial issues such as the behavior of the electric double layer in the electrochemical response are not affected by the test; (d) the presence of a self-evaluation process by the related causality factors is a crucial advantage that allows the scholar to assess the validity of the results and to proceed accordingly; (e) EFM can be the very first technique that can be applied on the specimen/sample surface without any previous treatment—in this way a very first and initial corrosion response is achieved that usually can represent the very worst scenario of a material's corrosion response; (f) EFM can be combined with CPP (Cyclic Potentiodynamic Polarization) and EIS (Electrochemical Impedance Spectroscopy) to provide a complementary, holistic approach to a system's electrochemical response.

2.3. Cyclic Potentiodynamic Polarization (CCP) Testing

Cyclic Potentiodynamic Polarization (CPP) is a robust, well-established technique for evaluating the electrochemical kinetics and localized corrosion susceptibility of metallic systems. In the present study, cyclic polarization was performed in a 3.5 wt.% NaCl solution, using a Gamry Reference 600 potentiostat/galvanostat with a three-electrode cell setup (Gamry Instruments, Warminster, PA, USA). The sample served as the working electrode, a graphite plate as the counter electrode, and a saturated calomel electrode (SCE) as the reference. Prior to the polarization tests, specimens were immersed for an hour to stabilize the open-circuit potential, followed by scanning at a rate of 10 mV/min. The pH was measured before and after the test and was found to be unchanged and close to a value of 7.

2.4. Electrochemical Impedance Spectroscopy (EIS)

The experiment was conducted using the same apparatus as was previously (Gamry) used. The excitation AC voltage was 10 mV amplitude relative to the OCP and the frequency scanning range was from 0.01 Hz to 100 kHz. A time interval of 60 s was adopted between the completion of the CPP test and the initiation of EIS for the OCP to be re-established.

3. Results

3.1. Phase Constitution Criteria and Crystal Structure

The phase selection in these systems can be rationalized through established HEA criteria. The δ parameter (atomic size difference) for these alloys remains within the range (typically < 6.6%) usually associated with solid solution formation. However, the most critical predictor for the FCC-to-BCC transition in this series is the Valence Electron Concentration (VEC) [6]. For the base CoCrFeNi, the VEC is high, favoring the FCC structure. As Ga (VEC = 3) replaces transition metals with higher VEC (e.g., Ni = 10, Co = 9), the overall VEC of the system drops.

For the Ga15 system, the calculated VEC is approximately 7.46, falling squarely into the 6.87 < VEC < 8.0 range where duplex FCC + BCC structures are predicted to coexist. The FeCoNiCrGa system reaches a VEC of approximately 7.20, further pushing the equilibrium toward the BCC phase. Additionally, the Ω parameter and ΔS_{mix} values for all three systems are sufficiently high to satisfy the requirements for stable high-entropy solid solutions, suppressing the formation of complex intermetallics in favor of the observed crystal structures.

Figure 1 illustrates the evolution of the crystal structure as Gallium is incrementally added to the CoCrFeNi matrix. The patterns represent the experimental data from the three distinct investigations. The XRD analysis of the base CoCrFeNi system confirms a predominant single-phase FCC structure, consistent with the literature for this medium-entropy system. The diffraction pattern shows prominent peaks at 2θ positions corresponding to the (111) (~44°), (200) (~51°), (220) (~75°) and (311) (~91°) planes of a single-phase Face-Centered Cubic (FCC) lattice. The high Valence Electron Concentration (VEC) of this system promotes the stability of the FCC solid solution. The presence of minor CrO_2 peaks was noted, likely a result of residual oxygen during the VAM process.

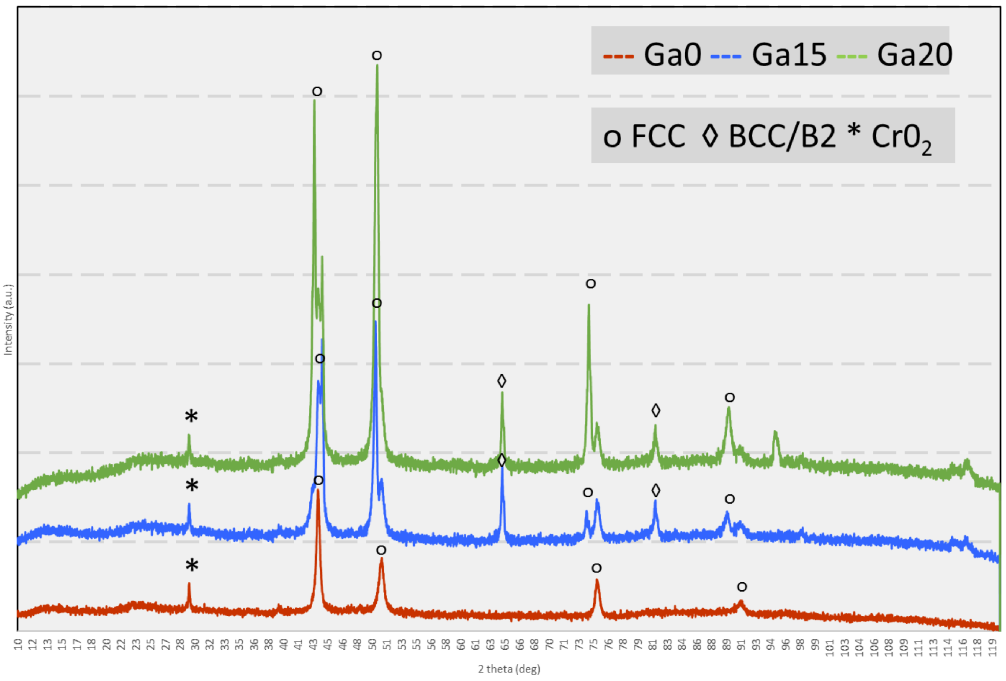

Figure 1. X-ray diffraction (XRD) patterns of Ga-doped alloys (Ga0, Ga15, and Ga20). The diffractograms illustrate the phase evolution as a function of Gallium.

Upon the introduction of 15 at.% Ga, the system presents a duplex structure (FCC + B2). The addition of Ga destabilizes the FCC phase and promotes the BCC/B2 phase. Crucially, secondary reflections begin to emerge, signifying the nucleation of a Body-Centered Cubic

(BCC) phase. Peak ~64.5° corresponds to the primary (211) reflection for the BCC/B2 phase, while peak ~82° matches the (210) or (220) reflections often seen in complex Ga-containing B2 structures. The system also shows a distinct shift in the FCC peaks toward lower angles, indicating an expansion of its lattice parameter. This aligns with a VEC of 7.46, which falls within the predicted range for mixed FCC + BCC phases. The lattice parameter of the FCC phase increases slightly with Ga addition, reflecting the lattice strain induced by the larger Ga atoms.

In the equiatomic FeCoNiCrGa system, the pattern reveals a robust duplex structure consisting of a dominant B2 phase with residual FCC. The "shoulders" on the peaks suggest significant lattice distortion as BCC peaks begin to overlap. The BCC peaks (typically (110) and (211)) are now clearly defined and comparable in intensity to the FCC reflections. The presence of low-intensity superlattice peaks also suggest an ordered B2 configuration within the BCC phase. The intensity of the BCC peaks is significantly higher compared to the Ga15 system, suggesting that the volume fraction of the BCC phase is directly proportional to the Gallium concentration. This structural evolution confirms Gallium's role as a BCC-stabilizing element in the transition metal matrix.

3.2. Microstructural Evolution

Figure 2 displays the Scanning Electron Microscopy (SEM) images comparing the as-cast morphologies of the three alloys. The base CoCrFeNi alloy (Figure 2a,b) exhibits a typical single-phase equiaxed or coarse grain structure in the as-cast state. SEM characterization confirms the absence of secondary phases, consistent with the predicted stability of the FCC solid solution for this medium-entropy transition metal alloy. The addition of 15 at.% Ga (Figure 2c,d) induces a fundamental morphological shift toward a dendritic structure, while in the equiatomic system (Figure 2e,f), the dendritic morphology is highly refined and the duplex nature is fully established.

Figure 3 uses Energy Dispersive Spectroscopy (EDS) to explain the chemical drivers of the phase transformation on all three cases. Figure 3a shows a highly homogeneous distribution of Co, Cr, Fe, and Ni in the base system with no significant segregation. It further confirms the absence of secondary phases or significant elemental segregation, consistent with the predicted stability of the FCC solid solution for the medium-entropy transition metal alloy.

As presented in Figure 3b, Ga and Ni are preferentially segregated into the interdendritic (BCC) regions, while Cr, Fe, and Co are enriched in the dendritic (FCC) cores. Figure 3b confirms the strong chemical affinity between Ni and Ga, which promotes the formation of the Ni-Ga-rich BCC/B2 phase. In contrast, the Ga15 alloy Figure 3c develops a well-defined dendritic morphology. EDS point analysis reveals that the dendritic cores (primary phase) are enriched in Cr, Fe, and Co, while the interdendritic regions are significantly enriched in Ni and Ga. This segregation pattern suggests that Ni and Ga have a lower partition coefficient in the FCC lattice, leading to their rejection into the liquid during solidification and the subsequent formation of the Ni-Ga-rich interdendritic phase.

The FeCoNiCrGa (Ga20) system displays a further refined dendritic structure. The elemental partitioning becomes even more pronounced, with the BCC phase (interdendritic) showing high concentrations of Ga and Ni, while the FCC phase (dendrites) remains rich in Cr and Fe. This microstructural evolution confirms that Gallium serves not only as a BCC stabilizer, but also as a primary driver for chemical partitioning, creating a composite-like microstructure that balances the properties of the ductile FCC and the harder BCC phases. These microstructural findings for the Ga15 and Ga20 systems are in agreement with the works of Sanchez-Carrillo et al. [17], Vida et al. [8], Wang et al. [29], and Molnar

et al. [9] who also supported the dual BCC/B2–FCC nature of the Ga-containing systems they examined.

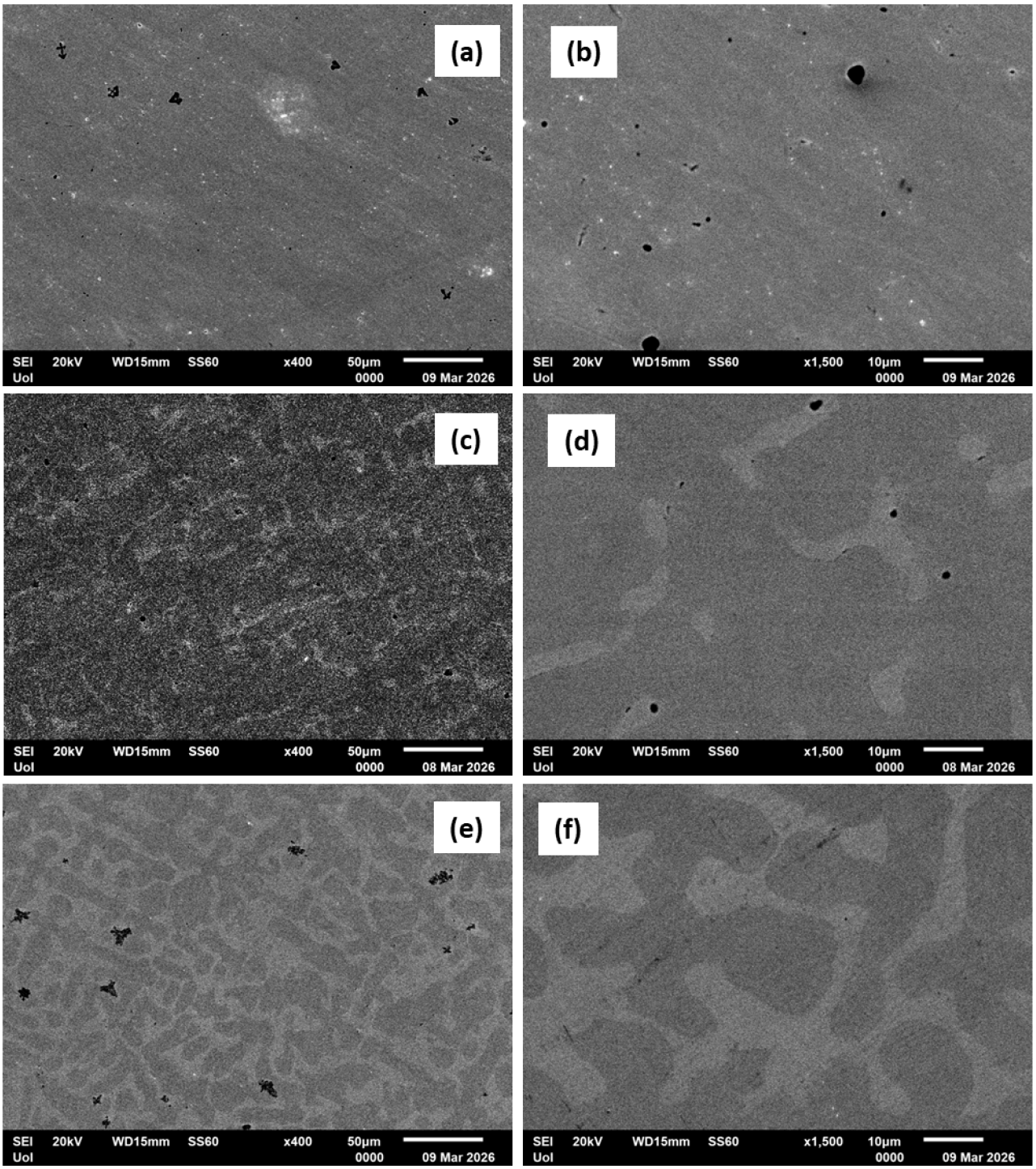

Figure 2. SEM images of (**a**,**b**) CoCrFeNi medium-entropy alloy, (**c**,**d**) (CoCrFeNi)85Ga15 high-entropy alloy, (**e**,**f**) (CoCrFeNi)80Ga20 high-entropy alloy at two different magnifications.

Image analysis revealed that the increase in the Ga content leads to an increase in the relative fraction of the Ga-rich phase, i.e., this fraction was calculated to be within the range of 18–22% for the Ga15 system whereas for the Ga20 system the corresponding fraction was increased up to a range of 31–34%.

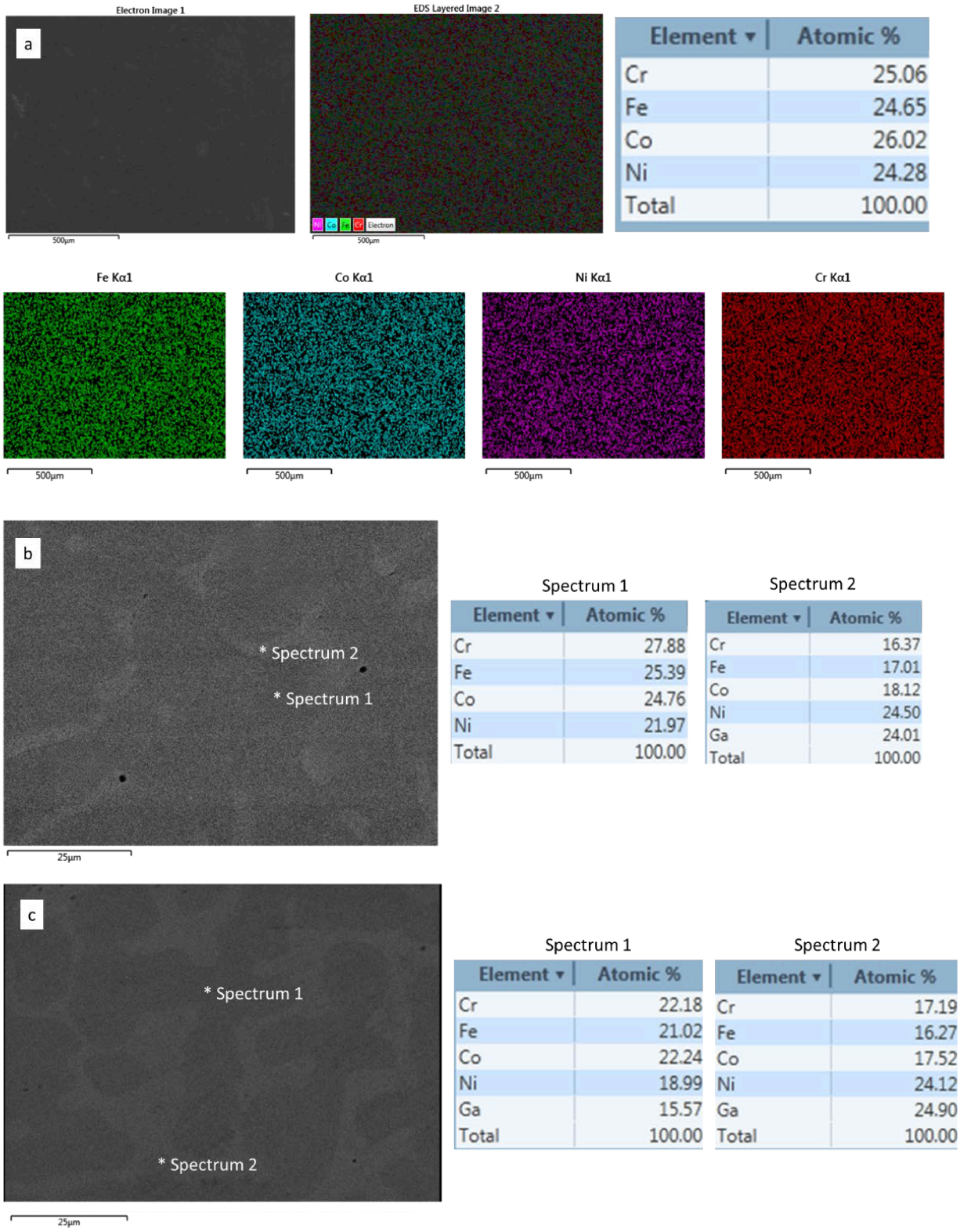

Figure 3. EDX analysis of (**a**) CoCrFeNi medium-entropy alloy, (**b**) (CoCrFeNi)85Ga15 high-entropy alloy, (**c**) (CoCrFeNi)80Ga20 high-entropy alloy.

3.3. Electrochemical Properties

3.3.1. Electrochemical Frequency Modulation (EFM) Results

In accordance with the theoretical framework established previously, Figure 4a–c illustrate the current response frequency spectra for the three alloy systems immersed in a 3.5 wt.% NaCl solution using excitation frequencies of 0.2 and 0.7 Hz. The spectra clearly

resolve the critical harmonic and intermodulation frequency components required for the kinetic calculations. Notably, these peaks exhibit high signal-to-noise ratios, remaining distinct and significantly elevated above the background noise floor. The electrochemical parameters derived from the EFM analysis are summarized and presented in Table 1.

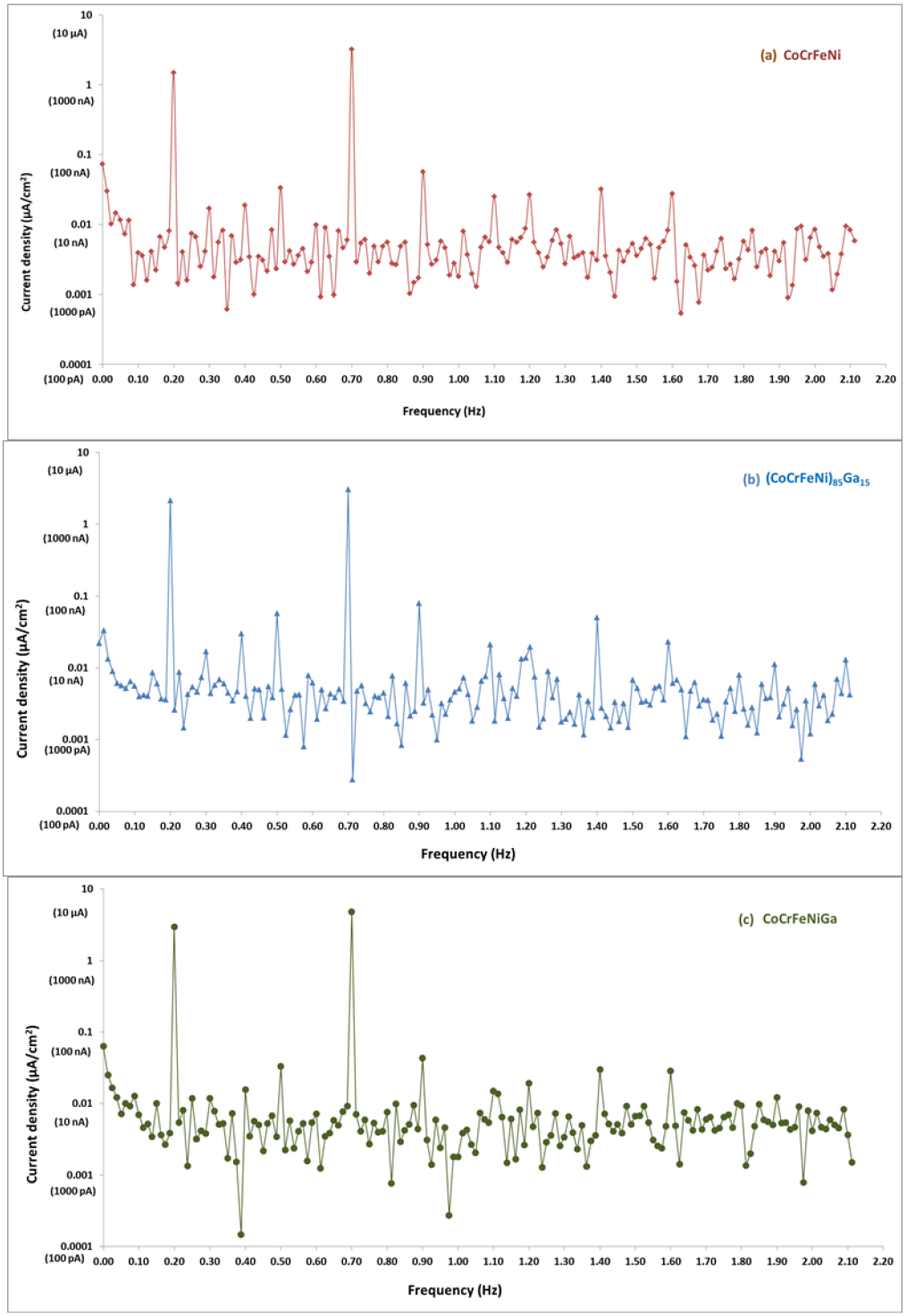

Figure 4. Frequency spectrum of the current response for the three different alloy systems in 3.5 wt. % NaCl solution and for the 0.2 and 0.7 Hz selected basic frequencies: (**a**) CoCrFeNi medium-entropy alloy, (**b**) (CoCrFeNi)85Ga15 high-entropy alloy, (**c**) (CoCrFeNi)80Ga20 high-entropy alloy.

Table 1. Various parameters calculated by the use of the EFM technique.

System	I_{corr} (μA/cm^2)	b_a (V/Decade)	b_c (V/Decade)	CF-2	Deviation % (CF-2)	CF-3	Deviation % (CF-3)	R_p (Ω)
CoCrFeNi	4.142	0.2151	0.2462	1.789	−10.55	2.629	−12.37	12,035
$(CoCrFeNi)_{85}Ga_{15}$	5.619	0.250	0.3127	1.711	−14.45	1.951	−35.00	10,736
$(CoCrFeNi)_{80}Ga_{20}$	10.01	0.3184	0.3522	1.686	−15.7	3.446	+14.87	7254

The experimental results consolidated in Table 1 reveal a distinct correlation between the stoichiometric composition of the alloy and its inherent electrochemical stability. Specifically, the corrosion current density (i_{corr}) scales proportionally with increasing Gallium content. This observation is further supported by the calculated polarization resistance (R_p) values, which undergo a concomitant reduction as the Ga concentration rises. From a kinetic standpoint, these data suggest that the incorporation of Ga into the quaternary CoCrFeNi matrix lowers the activation energy for charge transfer, thereby accelerating the anodic dissolution process. Furthermore, the presence of Ga appears to diminish the structural integrity and protective efficacy of the surface oxide film. Consequently, Ga substitution leads to a systematic degradation of the corrosion resistance relative to the baseline CoCrFeNi alloy.

The calculated causality factors (CF-2 and CF-3) reside within acceptable experimental thresholds, thereby validating the integrity of the EFM measurements. However, a progressive divergence from the ideal theoretical values CF-2 = 2 and CF-3 = 3) is observed in direct correlation with increasing Gallium concentration. The specific mechanisms driving these deviations are evaluated comprehensively in the Section 4. Critically, the EFM analysis was executed under the assumption of an activation-controlled (charge transfer) corrosion mechanism. This kinetic model was adopted a priori, as EFM constituted the initial stage of the experimental sequence, necessitating an assessment independent of the alloys' specific electrochemical profiles. While Kus and Mansfeld [27] posit that EFM precision can be optimized by the pre-selection of the governing operational mode (e.g., charge transfer, mass transport, or passivation), they concurrently acknowledge the inherent challenges of such a selection in complex, multi-component corrosion systems. These methodological considerations, along with their influence on the derived kinetic parameters, are addressed in detail in subsequent sections.

3.3.2. Cyclic Potentiodynamic Polarization (CPP) Results

Figure 5 illustrates the Cyclic Potentiodynamic Polarization (CPP) curves for the three investigated alloy systems in a 3.5 wt.% NaCl aqueous solution. A primary observation is that during the anodic forward scan, all specimens exhibit a direct transition from the Tafel region to a stable passive plateau, characterized by the absence of a distinct active-to-passive transition (anodic hump). This behavior indicates that the alloys undergo spontaneous passivation, whereby a stable, protective surface film is established at or near the corrosion potential (E_{corr}) [30,31]. The lack of a measurable critical current density (i_{crit}) further suggests that the kinetics of film formation are sufficiently rapid to preclude an active dissolution peak under the tested conditions.

Regarding the Ga0 and Ga20 systems, a discernible inflection in the current density is observed at potentials of 44.9 mV and 49.7 mV, respectively. Beyond these values, the current density exhibits an accelerated rate of increase over a narrow potential range. In contrast, such a transition is conspicuously absent in the Ga15 alloy. These transition points in the Ga0 and Ga20 systems have been subject to varying interpretations within the corrosion science community, often leading to methodological ambiguity. Certain studies classify these features as the breakdown potential (E_b), signifying the onset of passive film rupture [31–33]. Conversely, other researchers interpret these fluctuations as stochastic

instabilities inherent to the film formation process [30,34]. It should be noted, however, that a definitive breakdown point (E_b) is typically characterized by a sustained and sharp increase in current density following a stable passive plateau—a classic signature of the initiation and propagation of localized pitting corrosion [30,31].

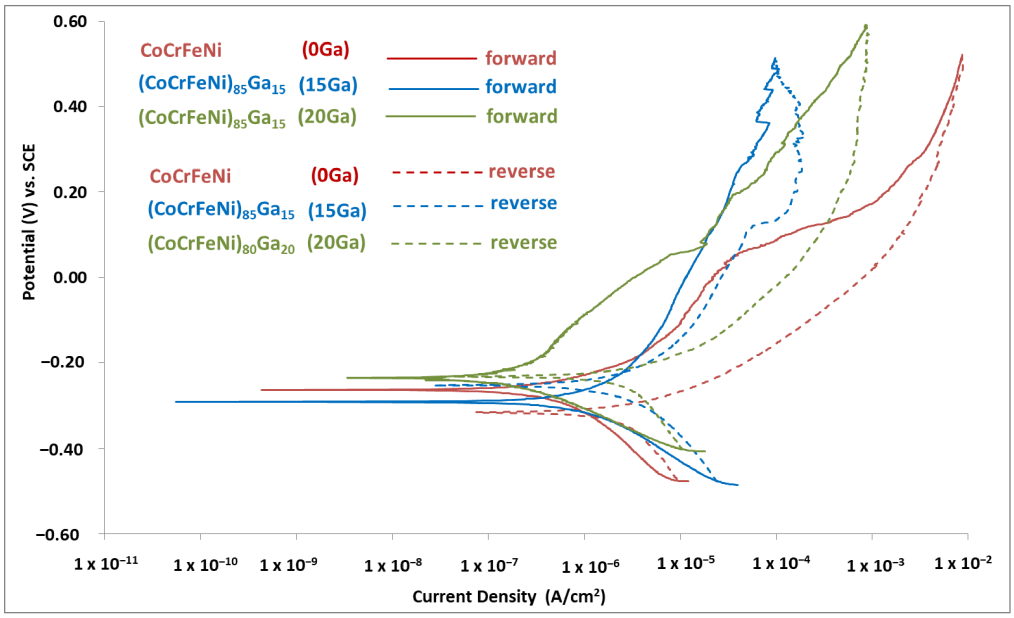

Figure 5. Cyclic polarization curves of the three different alloys.

However, such a definitive breakdown is not observed in the present study, at least within the context of the anodic forward polarization scan. No distinct, sharp plateau in current density—indicative of abrupt film rupture—is discernible. Consequently, the authors posit that while a passive film is established during the forward scan, its structural integrity and protective efficacy progressively diminish as the potential increases. In terms of discrete electrochemical parameters, the corrosion potentials recorded during the forward scan ($E_{corr,fwd}$) are −263 mV, −293 mV, and −235 mV for the Ga0, Ga15, and Ga20 systems, respectively. Based on these values, the Ga20 system exhibits the most positive $E_{corr,fwd}$, indicating a shift toward more noble thermodynamic behavior relative to the other compositions [8,30,32].

Analysis of the cathodic reverse scan provides a more comprehensive understanding of the alloys' electrochemical response. In all instances, a positive hysteresis loop is observed, characterized by reverse current densities that exceed those of the corresponding forward scan. The presence of these positive hysteresis loops serves as a robust indicator that localized corrosion has initiated and propagated [30,35]. The reverse corrosion potential ($E_{corr,rev}$) exhibits varying shifts relative to the forward values: for the Ga0 system, $E_{corr,rev}$ is more active at −316 mV; for Ga15, it is more noble at −252 mV; and for Ga20, it remains essentially unchanged at −239 mV. While the noble shift in the Ga15 system might initially suggest a degree of repassivation, the marginal magnitude of this potential difference, coupled with the overall positive hysteresis, renders such a conclusion tenuous. Typically, effective repassivation is marked by a $E_{corr,rev}$ that is several hundred millivolts more noble than $E_{corr,fwd}$ [35,36]. Consequently, the observed behavior across all compositions likely reflects a sustained susceptibility to localized attack rather than a significant self-healing capacity.

The presence of localized corrosion in all three different systems is further evidenced by the SEM examination of the corroded surfaces. Indeed, as shown in Figure 6, the presence of pits and localized corrosion traces can be observed for the different alloys.

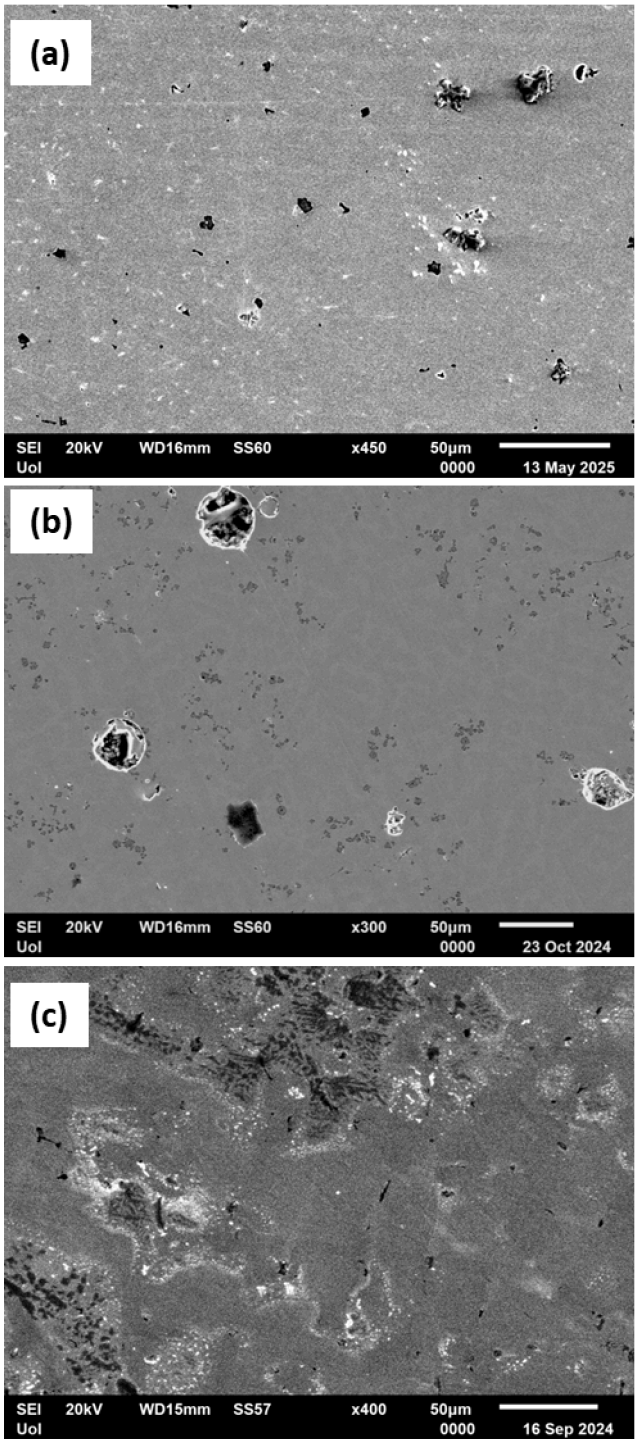

Figure 6. SEM images presenting panoramic views of the corroded surfaces after Cyclic Potentiodynamic Polarization (CPP) testing. In all cases the presence of pitting/localized corrosion is evident. (**a**) Ga0, (**b**) Ga15 and (**c**) Ga20 alloys respectively.

Table 2 consolidates the experimental data and derived parameters obtained from the Cyclic Potentiodynamic Polarization (CPP) measurements. Notably, the entries for the Ga20 alloy are denoted by an asterisk (*), indicating that these specific electrochemical parameters should be interpreted with caution. Specifically, during the numerical regression of the Tafel slopes using the Gamry analysis software, standard practice dictates that the selected regions of the anodic and cathodic branches be localized within an overpotential range of approximately ±100–150 mV relative to the open-circuit potential (E_{OC}) [37]. This constrained interval is recommended to ensure that the data points are extracted strictly

from the Tafel region, where a linear (or near-linear) relationship between potential and the logarithm of current density is maintained. Adherence to this criterion is fundamental to the validity of the Stern–Geary equation and ensures the reliability of the derived corrosion kinetic parameters [28].

Table 2. Electrochemical parameters after Cyclic Potentiodynamic Polarization (CCP).

Alloys	b_a	b_c	$E_{corr,fwd}$ (mV)	$E_{corr,rev}$ (mV)	I_{corr} (A/cm^2)	R_p (Ω)
CoCrFeNi (Ga0)	0.0567	0.0765	−263	−316	2.81×10^{-7}	50,319.93
$(CoCrFeNi)_{85}Ga_{15}$ (Ga15)	0.0552	0.0484	−293	−252	3.72×10^{-7}	30,101.47
$(CoCrFeNi)_{8Ga020}$ (Ga20) *	0.5442	0.1851	−235	−239	5.11×10^{-7}	117,366.43

* caution should be taken when consider the electrochemical parameter values (especially Rp) in the case of Ga20 system, as explained in the text.

In the present study, applying this Tafel extrapolation approach to the Ga20 system revealed a significant discrepancy between the calculated E_{corr} and the experimental E_{OC} within the prescribed ±100–150 mV overpotential range. Such a pronounced divergence between E_{OC} and E_{corr} is typically attributed to one of several factors:

1. Surface instability: High degrees of surface roughness or morphological irregularities on the working electrode.
2. Non-equilibrium conditions: An insufficiently stabilized E_{OC}, indicating that vigorous anodic or cathodic half-reactions were still active at the onset of the cyclic polarization scan.
3. Mass-transport limitations: The interference of diffusion-controlled phenomena that deviate from pure activation kinetics [38].

Given that the metallographic preparation was identical across all alloy systems and the E_{OC} was observed to stabilize in all instances, the origin of this irregularity likely resides in intrinsic material phenomena, such as surface inhomogeneities or diffusion-limited charge transfer. Consequently, the kinetic parameters derived for the Ga20 alloy must be interpreted with significant reservation, as they may not fully reflect a purely activation-controlled mechanism.

Data in Table 2 indicate that i_{corr} values increase monotonically with Gallium concentration. This trend suggests that higher Ga content systematically compromises the alloy's corrosion resistance. However, this phenomenon is not uniformly reflected in the polarization resistance (R_p) values, which typically exhibit a reciprocal proportionality to i_{corr} according to the Stern–Geary relationship. Notably, in the Ga20 system, despite exhibiting the highest i_{corr}, the R_p value calculated via the Stern–Geary equation is paradoxically the highest among the investigated alloys. This mathematical contradiction is a direct consequence of the localized instabilities and non-ideal Tafel behavior discussed previously. The lack of an established linear activation region for this specific composition likely introduces significant error into the R_p calculation, necessitating a cautious interpretation of these derived kinetic parameters.

A final noteworthy observation derived from the Cyclic Potentiodynamic Polarization (CPP) curves in Figure 5 concerns the cathodic current densities at the termination of the reverse scan. While the Ga0 alloy generally exhibits the highest current densities during the anodic forward polarization, it conversely demonstrates the lowest current density at the conclusion of the cyclic test. This observation is critical because the final potential and current state represent the immediate surface condition of the specimens prior to Electrochemical Impedance Spectroscopy (EIS). Since EIS constitutes the final phase of the experimental sequence, the relative stability and localized current distribution at this

terminal stage will directly influence the subsequent impedance response, as discussed in detail in the following section.

3.3.3. Electrochemical Impedance Spectroscopy (EIS)

Figure 7 illustrates the Nyquist plots for the various alloy systems under investigation. In all instances, the shape of the curves can be characterized as suppressed towards the *x*-axis semicircle arcs. This morphology is typically attributed to charge transfer processes occurring on stochastic or inhomogeneous surface facets [30,31,34,35,39]. The degree of depression within the arc correlates with the intensity of the charge transfer heterogeneity, whereas a more idealized semicircular geometry signifies dominant capacitive behavior. To mathematically account for this divergence from ideal capacitance, Constant Phase Elements (CPEs) are incorporated into the equivalent electrical circuit (EEC) modeling. The n-values associated with these CPEs quantify the deviation from pure capacitive response. A qualitative analysis of the plots reveals that the quaternary (Ga0) system possesses the largest polarization diameter, indicating superior corrosion resistance relative to the Ga-bearing alloys. A comparison between the Ga15 and Ga20 systems further corroborates that increased Ga concentration facilitates a reduction in total impedance. Notably, both Ga-modified alloys exhibit a characteristic "tail" in the low-frequency regime, which is symptomatic of diffusion-controlled kinetics. This mass-transport phenomenon is subsequently modeled using a Warburg impedance element within the proposed equivalent circuit [32,40–42].

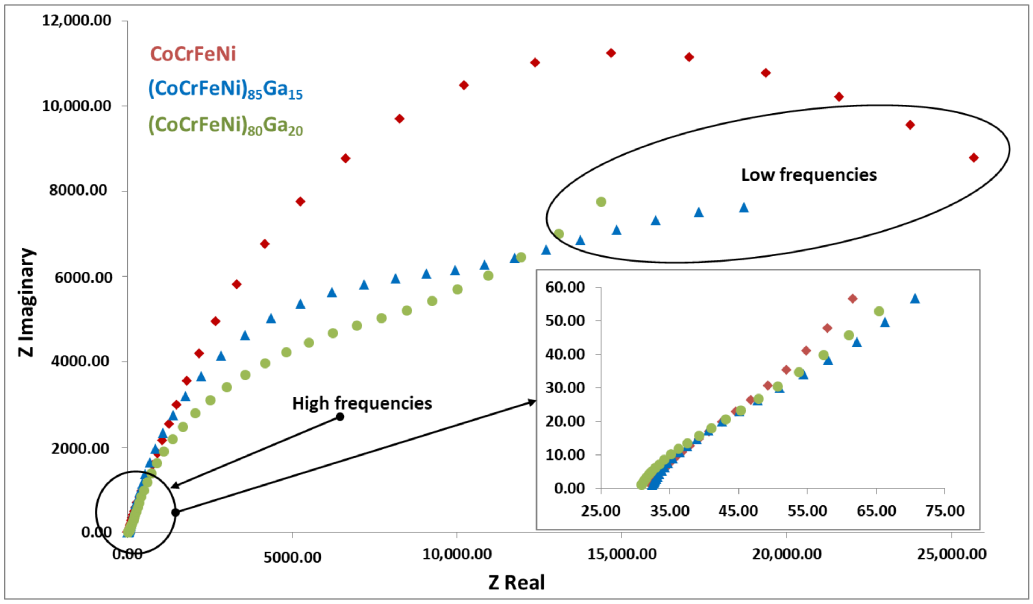

Figure 7. Nyquist plots of the different systems. The insert graph presents the Z real and Zimag curves at low frequencies.

The inset in Figure 7 illustrates the complex impedance relationship Z_{imag}–Z_{real}) within the high-frequency regime. A secondary depressed capacitive loop is clearly discernible at these frequencies, necessitating the incorporation of an additional Constant Phase Element (CPE) into the equivalent electrical circuit (EEC) to accurately model the electrochemical response. The requirement for a second time constant is consistent with previous investigations, such as those by Suang et al. [34], Shi et al. [31], and Yakanaka et al. [30]. Physically, this dual-CPE architecture reflects a heterogeneous surface state characterized by a mixed response from passive film regions and localized features such as pits or other morphological inhomogeneities. These high-frequency features provide the mechanistic basis for

constructing a representative EEC that accounts for both the dielectric properties of the passive layer and the charge transfer kinetics at active sites.

Figure 8 displays the corresponding Bode plots, illustrating the impedance magnitude ($Z_{modulus}$) and phase angle shift as a function of frequency. These spectra provide further validation of the trends observed in the Nyquist plots. The impedance magnitude in the low-frequency limit is highest for the quaternary (Ga0) system, followed by the Ga15 alloy, while the Ga20 system exhibits the lowest $Z_{modulus}$ values. These disparities are most pronounced in the low-frequency regime, reinforcing the conclusion that corrosion resistance undergoes systematic degradation with increasing Gallium concentration. Furthermore, at lower frequencies, the $Z_{modulus}$ profile exhibits a modified slope corresponding to a phase angle shift of approximately 40°. This feature serves as a diagnostic indicator of a diffusion-controlled mechanism (Warburg impedance). While an ideal, semi-infinite linear diffusion process yields a theoretical phase shift of 45°, the observed deviation suggests a mixed-control regime where a partial charge-transfer character is maintained alongside mass-transport limitations.

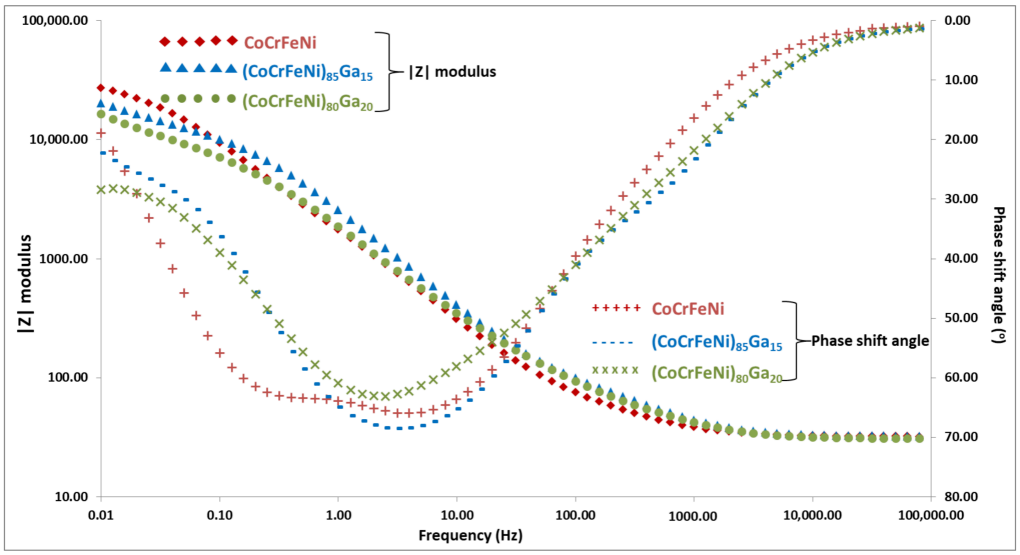

Figure 8. Comparative plot presenting the corresponding Bode ($Z_{modulus}$ vs. frequency and phase angle shift vs. frequency respectively).

(A) Electric circuit construction

To further interpret the electrochemical response, various equivalent electrical circuit (EEC) models were designed based on the analysis of the Nyquist and Bode plots, integrated with the prior observations from CPP testing. The empirical evidence suggests that the electrochemical interface can be modeled as a porous passive film coupled with the characteristics of the electrical double layer. This modeling approach is well-established in the literature [29–31,35,39,40,43–48] and typically incorporates the following parameters: R_s (solution/electrolyte resistance), R_{film} (ohmic resistance of the passive layer), CPE_{film} (Constant Phase Element representing the capacitive response of the film while accounting for surface inhomogeneities), R_{ct} (charge transfer resistance across the double layer) and CPE_{dl} (Constant Phase Element describing deviations from ideal capacitive behavior at the double layer).

For the Ga15 and Ga20 alloy systems, which exhibited signs of diffusion-controlled kinetics, the model was refined by incorporating a Warburg impedance element. This modification is consistent with similar refinements reported in other studies [32,40,41,45,49] to account for mass-transport limitations. Consequently, the proposed equivalent circuit

for the quaternary CoCrFeNi alloy is illustrated in Figure 9 (MODEL A), representing the baseline configuration without diffusion-limited components.

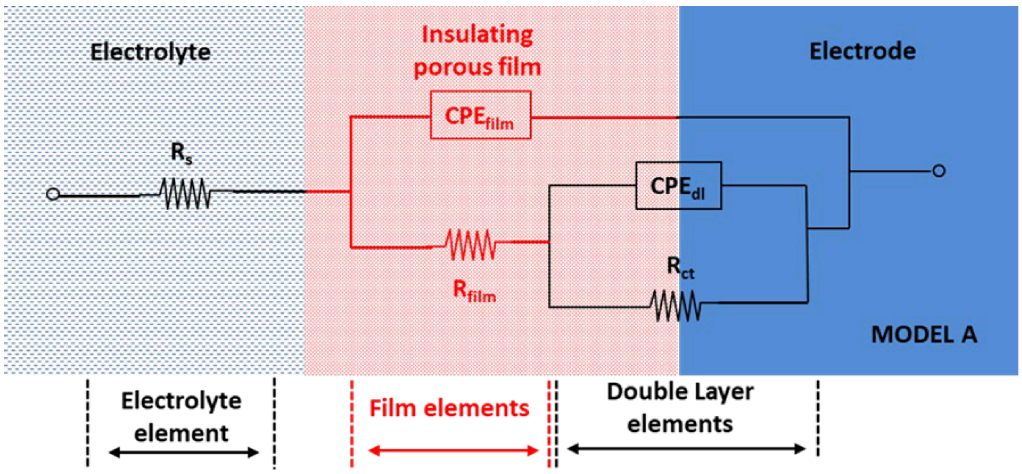

Figure 9. The electric circuit (MODEL A) adopted for the quartenary CoCrFeNi medium-entropy alloy.

Figure 10 illustrates the modified equivalent electrical circuit (MODEL B) specifically developed for the Ga15 and Ga20 alloy systems. The integration of a Warburg impedance element is clearly observed, serving to account for the diffusion-limited mass transport phenomena identified during the experimental analysis. Furthermore, to describe the non-ideal capacitive response of the system, a Constant Phase Element (CPE) was employed. The impedance of the CPE (Z_{CPE}) is mathematically defined by the following expression:

$$Z_{CPE} = Y_0^{-1}(j\omega)^{-a} \quad (7)$$

where:

Y_0 is the admittance (Scm-2sa);

j is the imaginary number;

ω is the angular frequency (rads^{-1});

a is a dimensional variable which represents the diversity of CPE from the pure capacitive behavior. Notably, if $\alpha = 0$ then CPE represents a resistance with $R = Y_0{}^{-1}$, for $\alpha = 1$ CPE represents a capacitance with $C = Y_0$, and for $\alpha = 0.5$ CPE represents a Warburg element [25]. The Warburg element impedance is provided by Equation (8):

$$Z_W = \sigma\omega^{-\frac{1}{2}}(1 - j) \quad (8)$$

where

$$\sigma = \frac{RT}{n^2F^2A\sqrt{2}}\left(\frac{1}{C_0^*\sqrt{D_0}} + \frac{1}{C_R^*\sqrt{D_R}}\right) \quad (9)$$

where:

R, F—the gas and Faraday constants;

A—the electrode surface;

n—the number of transferred electrons;

D—the diffusion coefficient;

C*—the concentration within the bulk;

O and R—the oxidized and the reduced species respectively.

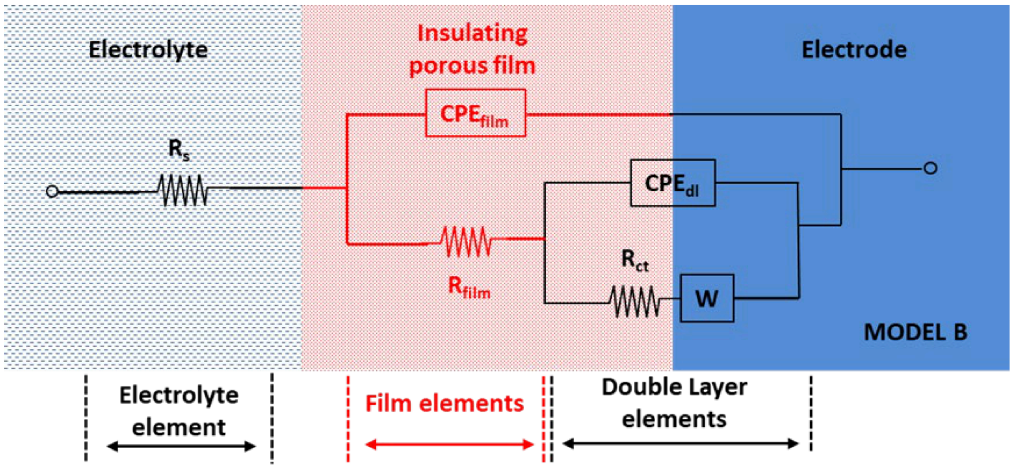

Figure 10. The equivalent electric circuit (MODEL B) used to describe the behavior of alloys Ga15 and Ga20. Notice the presence of the Warburg element to take account for the diffusion process phenomena.

To ensure the highest degree of reliability in the fitting of the electrochemical data for the Ga15 and Ga20 alloys, and to validate the selection of the most appropriate equivalent electrical circuit (EEC), the authors also evaluated the modeling approach proposed by Luo et al. [50] and Hermas and Morad [51]. In this alternative configuration, the traditional Warburg impedance element was replaced with a Constant Phase Element (CPE) to specifically account for diffusion-limited processes, hereafter designated as CPE_{diff}. Consequently, an alternative EEC (MODEL C) was developed and evaluated, as illustrated in Figure 11.

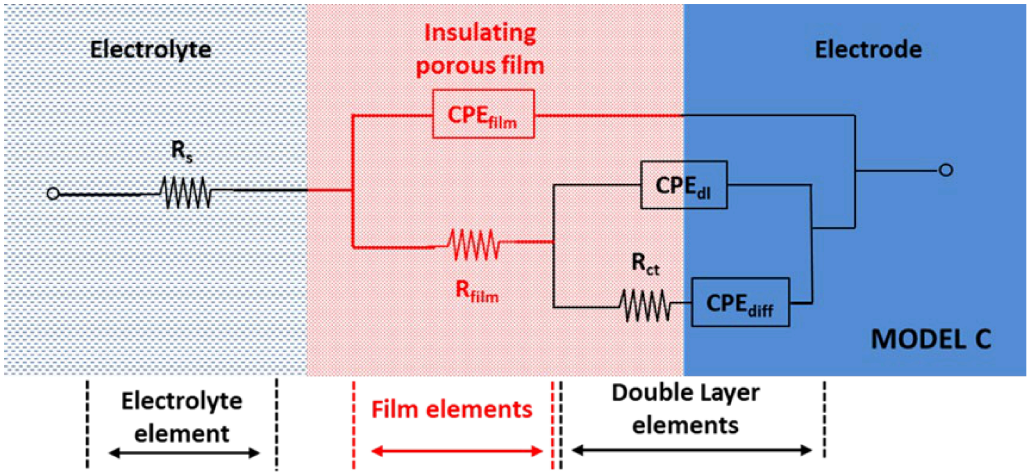

Figure 11. Alternative equivalent electric circuit (MODEL C) to evaluate the electrochemical response of Ga15 and Ga20 alloys. The Warburg element has been substituted by a new CPE_{diff} element to account for the diffusion phenomena.

(B) Equivalent electric circuit model fitting

The fitting of the proposed equivalent electrical circuits was performed utilizing the Gamry Echem Analyst software suite, which enabled the simultaneous extraction of all relevant electrochemical parameters. The statistical reliability and physical validity of the proposed models were rigorously assessed through the "goodness of fit" parameter provided by the software. The comprehensive set of derived data, including the resistance, capacitance, and diffusion coefficients for each alloy system, is summarized in Table 3.

Table 3. Calculated parameters and goodness of fitting for the different equivalent circuits used for the different alloy systems.

CoCrFeNi	**MODEL A**	**Parameters**	Values	Error (%)	Goodness of fitting
		$\mathbf{R_s}$ **(ohm)**	31.85	1.05	755.6×10^{-6}
		$\mathbf{R_{film}}$ **(ohm)**	79.95	8.76	
		$\mathbf{Y_{film}}$	80.59×10^{-6}	4.37	
		$\boldsymbol{\alpha_{film}}$	0.785	7.05	
		$\mathbf{R_{ct}}$ **(ohm)**	22,620	2.23	
		$\mathbf{Y_{dl}}$	51.95×10^{-6}	7.09	
		$\boldsymbol{\alpha_{dl}}$	0.785	0.87	
$\mathbf{(CoCrFeNi)_{85}Ga_{15}}$	**MODEL B**	**Parameters**	Values	Error (%)	Goodness of fitting
		$\mathbf{R_s}$ **(ohm)**	32.17	1.16	276.0×10^{-6}
		$\mathbf{R_{film}}$ **(ohm)**	109.1	6.00	
		$\mathbf{Y_{film}}$	40.32×10^{-6}	2.44	
		$\boldsymbol{\alpha_{film}}$	0.866	4.35	
		$\mathbf{R_{ct}}$ **(ohm)**	12,970	3.63	
		$\mathbf{Y_{dl}}$	37.44×10^{-6}	2.65	
		$\boldsymbol{\alpha_{dl}}$	0.818	4.99	
		$\mathbf{W_{dl}}$	425.0×10^{-6}	6.70	
	MODEL C	**Parameters**	Values	Error(%)	Goodness of fitting
		$\mathbf{R_s}$ **(ohm)**	32.25	1.25	229.5×10^{-6}
		$\mathbf{R_{film}}$ **(ohm)**	105.6	6.15	
		$\mathbf{Y_{film}}$	41.55×10^{-6}	2.44	
		$\boldsymbol{\alpha_{film}}$	0.868	4.11	
		$\mathbf{R_{ct}}$ **(ohm)**	11,380	8.30	
		$\mathbf{Y_{dl}}$	34.32×10^{-6}	2.84	
		$\boldsymbol{\alpha_{dl}}$	0.829	5.52	
		$\mathbf{Y_{diff}}$	295.3×10^{-6}	4.85	
		$\boldsymbol{\alpha_{diff}}$	0.406	4.70	
$\mathbf{(CoCrFeNi)_{80}Ga_{020}}$	**MODEL B**	**Parameters**	Values	Error (%)	Goodness of fitting
		$\mathbf{R_s}$ **(ohm)**	30.51	1.33	470.6×10^{-6}
		$\mathbf{R_{film}}$ **(ohm)**	114.1	8.59	
		$\mathbf{Y_{film}}$	63.14×10^{-6}	2.87	
		$\boldsymbol{\alpha_{film}}$	0.781	5.73	
		$\mathbf{R_{ct}}$ **(ohm)**	10,710	1.95	
		$\mathbf{Y_{dl}}$	59.33×10^{-6}	2.89	
		$\boldsymbol{\alpha_{dl}}$	0.776	6.72	
		$\mathbf{W_{dl}}$	480.6×10^{-6}	6.63	
	MODEL C	**Parameters**	Values	Error(%)	Goodness of fitting
		$\mathbf{R_s}$ **(ohm)**	30.51	1.36	476.9×10^{-6}
		$\mathbf{R_{film}}$ **(ohm)**	134.0	9.08	
		$\mathbf{Y_{film}}$	54.22×10^{-6}	3.43	
		$\boldsymbol{\alpha_{film}}$	0.802	6.5	
		$\mathbf{R_{ct}}$ **(ohm)**	10,060	6.76	
		$\mathbf{Y_{dl}}$	66.98×10^{-6}	2.84	
		$\boldsymbol{\alpha_{dl}}$	0.765	6.49	
		$\mathbf{Y_{diff}}$	413.3×10^{-6}	6.04	
		$\boldsymbol{\alpha_{diff}}$	0.4626	5.02	

In all instances, the goodness-of-fit values remained within the magnitude of 10^{-6}, demonstrating excellent statistical agreement. Such low values indicate a high degree of precision and substantiate the reliability of the simulations performed between the experimental datasets and the respective equivalent electrical circuits [29–32,34,40,41,44,45,48,52].

In the cases of the Ga15 and Ga20 alloys, both Model B (incorporating a Warburg impedance element) and Model C (utilizing a CPE_{diff} element) yielded comparable results with negligible differences in the goodness-of-fit parameters. However, the methodology proposed by Hermas and Morad [51] and Luo et al. [50], which substitutes the traditional Warburg element with a Constant Phase Element to better account for non-ideal diffusion layers, demonstrated high statistical reliability. Consequently, this study adopted Model C as the primary framework for analyzing the Gallium-containing systems.

The ohmic resistance components of the equivalent electrical circuits (EECs) provide the basis for calculating the total polarization resistance (R_p) of each system. R_p represents the resistance of the electrode surface to polarization upon contact with the electrolyte and serves as a fundamental quantitative metric for an alloy's electrochemical corrosion resistance in a given environment [30,40]. Given that the ohmic elements within the proposed circuit models are arranged in series, the total R_p is derived from the summation of all individual resistive components [30,40]. Accordingly, the total polarization resistance is defined by the following expression:

$$R_p = R_s + R_{film} + R_{ct} \quad (10)$$

(C) Parameter calculations for the electric circuit model

While a direct comparative analysis between Model A and Models B and C is necessitated by the varying degrees of freedom in their respective circuit architectures, several critical trends across the alloy series remain discernible:

a. Solution resistance (R_s): Across the entire alloy series and independent of the selected equivalent electrical circuit (EEC) topology, the R_s values exhibit negligible variation. This consistency confirms that the ionic conductivity of the electrolyte remained stable throughout the electrochemical characterization, ensuring that fluctuations in total impedance are attributable solely to interfacial phenomena rather than bulk solution changes.

b. Passive film properties: The ohmic resistance of the porous passive film (R_{film}) exhibited a progressive increase with Gallium content, rising from 79.95 Ohms for the Ga0 alloy to 105.6 Ohms for the Ga15 system, and reaching 134.0 Ohms for the Ga20 system. Concurrently, the film admittance (Y_{film}) fluctuated from 80.59×10^{-6} (Ga0) to 40.32×10^{-6} (Ga15) and 54.22×10^{-6} (Ga20). The associated a_{film} exponents, which reflect surface homogeneity, were determined to be 0.785, 0.868, and 0.802, respectively.

c. Charge transfer kinetics: A pronounced trend is observed in the electrical double-layer characteristics, specifically regarding the charge transfer resistance (R_{ct}) since it decreased sharply from 22,620 Ω in the base Ga0 alloy to 11,380 Ω for the Ga15 alloy, and further to 10,060 Ω for the Ga20 system, indicating a degradation in the overall corrosion resistance as Gallium concentration increases.

d. Diffusion phenomena: In the Ga15 and Ga20 alloys, where mass-transport limitations were evident, the impedance parameters varied significantly depending on the model selection. Under Model B, the Warburg impedance coefficient increased from 425.0×10^{-6} for Ga15 to 480.6×10^{-6} for Ga20. However, Model C—selected for its superior physical representation of these alloys—revealed more pronounced differences. Specifically, the diffusion-related admittance (Y_{diff})

rose from 293.5 × 10^{-6} (Ga15) to 413.3 × 10^{-6} (Ga20), with corresponding a_{diff} exponents of 0.406 and 0.4626, respectively.

Based on Equation (10) and given the adoption of Model C for the Ga15 and Ga20 systems, the calculated polarization resistance (Rp) values are 22,731.8 Ω, 11,587.85 Ω, and 10,324.51 Ω for the Ga0, Ga15, and Ga20 alloys, respectively. A clear correlation is observed: Rp decreases progressively as the Gallium concentration increases. This significant reduction in Rp signifies that the incorporation of Ga facilitates charge transfer and compromises the protective integrity of the passive film, thereby deteriorating the overall electrochemical corrosion resistance of the foundational quaternary CoCrFeNi alloy.

3.4. Comparison Between the Different Electrochemical Techniques' Outcomes

A comparative analysis of the outcomes derived from the various electrochemical techniques is essential to ensure data consistency and phenomenological validation. Table 4 consolidates the calculated polarization resistances (R_p) and the total impedance moduli for each method, both of which serve as quantitative metrics for the alloys' corrosion resistance. Based on the data presented in Table 4, the following comparative remarks regarding the efficacy and correlation of the different characterization methods can be elucidated:

(a) Electrochemical Frequency Modulation (EFM) was conducted on the pristine, unperturbed specimen surfaces, ensuring that no prior electrochemical or mechanical treatments altered the initial interfacial characteristics. Consequently, the parameters derived from EFM represent the most conservative baseline—effectively a "worst-case" scenario—for the alloy's inherent corrosion resistance prior to the development of a steady-state passive film. The data consistently follow a trend wherein increased Gallium concentration facilitates a systematic reduction in corrosion resistance, reinforcing the observations made across other characterization techniques.

(b) In contrast, Cyclic Potentiodynamic Polarization (CPP) provides a more idealized representation of the alloy's corrosion resistance. This inherent bias arises because the kinetic parameters are extrapolated from the activation-controlled Tafel region during the anodic forward scan. Consequently, this method fails to account for the terminal state of the electrode surface following the reverse scan, where localized damage may have accumulated. For the Ga20 alloy specifically, a notable divergence in the data trend is observed; this is largely attributable to the presence of mass-transport limitations, which cannot be accurately resolved using standard CPP Tafel extrapolation.

(c) Electrochemical Impedance Spectroscopy (EIS) was executed as the terminal phase of the experimental sequence. Unlike transient techniques, EIS provides a holistic characterization of the interface, accounting for the cumulative effects of all active electrochemical phenomena. Furthermore, the impedance response reflects the final steady-state condition of the electrode surface following the preceding polarization protocols.

(d) EFM and EIS utilize a fundamentally different methodology for evaluating corrosion kinetics compared to the CPP technique. By employing small-amplitude alternating current (AC) signals across a spectrum of frequencies, EFM and EIS enable the resolution of complex interfacial phenomena. In contrast, the conventional CPP method relies on a direct current (DC) sweep, which lacks the frequency-dependent resolution necessary to isolate double-layer characteristics from the total polarization response. These methodological distinctions, along with broader considerations regarding the comparative validity and limitations of diverse electrochemical techniques, have been extensively discussed in the literature by Obot et al. [8,14] and Harrington et al. [50,53].

In conclusion, the authors believe that these electrochemical techniques yield indispensable qualitative and quantitative insights into the corrosion mechanisms of complex

alloy systems. A synergistic interpretation of data derived from both potentiodynamic and frequency-domain measurements establishes a robust framework for defining property margins. Consequently, this integrated methodological approach is essential for the rational design of novel alloys with tailored and predictable electrochemical performance.

Table 4. R_p and Z moduli calculated for the different electrochemical methods.

System	CoCrFeNi (Ga0)		(CoCrFeNi)85Ga15 (Ga15)		(CoCrFeNi)8Ga020 (Ga20)	
Method	**Rp (Ω)**	**Zmodulus (Ω)**	**Rp (Ω)**	**Zmodulus (Ω)**	**Rp (Ω)**	**Zmodulus (Ω)**
EFM	12,035	- *	10,736	- *	7254	- *
CPP	50,319.9	- *	30,101.5	- *	117,366	- *
EIS	22,731.9	27,139	11,587.9	20,279.5	10,324.5	16,341

* Not calculated by the EFM and CPP methods.

4. Discussion

4.1. Metallurgical Mechanisms of Ga Addition

The transition from FCC to BCC upon Ga addition is a classic example of electronic and geometric stabilization. Gallium possesses a larger atomic radius than Co, Cr, Fe, or Ni, which induces significant local lattice distortion (the "lattice distortion effect"). This distortion increases the internal strain energy of the FCC lattice. The system compensates by forming the more "open" BCC structure, which can better accommodate larger atoms. Furthermore, the chemical affinity between Ni and Ga is exceptionally high, as evidenced by the negative enthalpy of mixing (ΔH_{mix}) between these two elements. This affinity drives the segregation of Ni and Ga into the interdendritic spaces. The resulting interdendritic phase is not merely a disordered BCC but likely an ordered B2 phase, which is commonly observed in Al- or Ga-doped HEAs. This duplex nature provides a "cocktail effect", where the FCC matrix provides ductility while the BCC/B2 phase provides significant strengthening.

4.2. Electrochemical Frequency Modulation (EFM)

Notably, the literature regarding the application of Electrochemical Frequency Modulation (EFM) to conventional and advanced alloy systems remains sparse; specifically, its implementation for high-entropy alloys (HEAs) is, to the authors' knowledge, nearly non-existent.

As detailed in the Results section of this study, increasing Gallium concentration facilitates a systematic degradation of corrosion resistance, a trend clearly reflected in the derived kinetic parameters. Furthermore, the morphology and relative intensities of the primary intermodulation peaks observed in the response signal (illustrated in Figure 4 demonstrate strong qualitative agreement with the spectral profiles reported in the seminal works of Abdel-Rehim et al. [54] and Khaled et al. [55]. This consistency validates the applicability of EFM as a non-destructive tool for monitoring the instantaneous corrosion rates of these complex alloy systems.

The calculated causality factors (CF-2 and CF-3) fall within the theoretically acceptable ranges established by Abdel-Rehim et al. [54], Obot and Onyeachu [14], Bosch et al. [19], and Kus and Mansfeld [27]. It was observed, however, that the deviation of these factors from their ideal values of 2.0 and 3.0, respectively, increased in correlation with Gallium concentration. The literature suggests that such discrepancies typically arise from interfacial inhomogeneities, rapid repassivation kinetics, or mass-transport limitations (diffusion) at the electrode–electrolyte interface [14,19,27]. Consequently, as noted by Kus et al. [27], the investigator must determine the predominant corrosion mechanism—a task that is often non-trivial and mathematically demanding. Given the lack of prior electrochemical data

for this specific alloy system, the authors adopted an activation-controlled (charge transfer) model for the EFM analysis. Considering that EFM served as the initial diagnostic step in this experimental sequence, this approach was deemed the most appropriate baseline for evaluating the fundamental kinetic response.

In accordance with the established literature [14,19,27,54,55], it is widely recognized that while Electrochemical Frequency Modulation (EFM) yields critical kinetic data, it is insufficient as a standalone technique for a comprehensive assessment of a system's corrosion behavior. To achieve a holistic understanding of the interfacial mechanisms, EFM data must be corroborated by Cyclic Potentiodynamic Polarization (CPP) and/or Electrochemical Impedance Spectroscopy (EIS). Consequently, this multi-technique approach was adopted in the present study to provide a rigorous and cross-validated characterization of the alloys' electrochemical response.

4.3. Cyclic Potentiodynamic Polarization (CPP)

In the current study, parameters derived from the Tafel extrapolation region revealed a negative shift in the corrosion potential (E_{corr}) and a concomitant increase in corrosion current density (i_{corr}) as the Gallium concentration increased. Furthermore, all alloy compositions exhibited a positive hysteresis loop upon scan reversal, with no discernible repassivation potential (E_{rp}) or tendency for surface recovery. These electrochemical signatures collectively indicate a high susceptibility to pitting nucleation and propagation. The sole divergence in the dataset—where the polarization resistance (R_p) did not strictly correlate with the i_{corr} trend—was addressed in the preceding Section 3 through a consideration of the non-linearities in the activation-controlled region.

To gain a more comprehensive understanding of the systems' behavior during Cyclic Potentiodynamic Polarization (CPP), a detailed analysis of the individual polarization stages is required. Immediately following the activation-controlled Tafel region, all alloy compositions transition into a passive regime during the anodic forward scan, characterized by the formation of a protective surface oxide film. The morphology of the potential–current (E-I) curve within this domain yields critical insights into the interfacial kinetics. As established by Megremis [56], the potentiostatic slope in this region serves as a quantitative metric for the competing rates of metallic dissolution and passive film growth. Consequently, this slope elucidates the kinetics governing the stability of the passivating layer, where a steeper gradient typically signifies a more robust and protective film architecture.

From this perspective, the anodic polarization curves reveal that the Ga0 alloy exhibits the lowest slope, followed by the Ga20 system, while the Ga15 alloy possesses the highest gradient. Mechanistically, the steeper slope observed in the Ga15 alloy signifies a suppressed metallic dissolution rate and an enhanced rate of passive film nucleation and stability. Interestingly, this trend is accompanied by generally higher passive current densities in the post-Tafel region of the forward scan. This observation is critical; while the parameters derived from the Tafel extrapolation initially identified the Ga0 alloy as having the superior corrosion resistance (lowest i_{corr}), this performance advantage does not persist across the broader potential range of the forward scan. This suggests that while the Ga0 system is more stable at its open-circuit potential (OCP), its passive film integrity may be inferior to that of the Ga15 alloy under increasing anodic overpotentials.

An additional paradox arising from the preceding discussion concerns the role of Chromium (Cr). It is widely established in the literature [30,31,34,35,57] that Cr facilitates the formation of highly stable passive films, primarily composed of Cr_2O_3 oxides and, under certain conditions, hydroxides, which significantly enhance corrosion resistance. In the present study, the Cr content is reduced in the Ga15 and Ga20 alloys; theoretically, this depletion should result in a more pronounced degradation of corrosion resistance relative

to the quaternary CoCrFeNi baseline. However, the opposite phenomenon was observed during the anodic forward scan: the CoCrFeNi alloy exhibited the poorest performance in the passive regime. This discrepancy necessitates a deeper investigation into the synergistic effects of Ga on film stability.

Fu et al. [58] postulated that the high-entropy effect, characterized by sluggish diffusion and the cocktail effect inherent to HEAs, is a primary driver for enhanced corrosion resistance. This is attributed to two main factors: (a) the suppression of elemental segregation, which mitigates the formation of micro-galvanic cells that typically trigger pitting, and (b) the facilitation of a more homogeneous and stable passive film.

Under this framework, the Ga15 and Ga20 alloys, possessing higher configurational entropy, should theoretically exhibit improved electrochemical stability. However, Fu et al. [58] also cautioned that entropic effects alone are insufficient to dictate corrosion behavior, as the presence of secondary or multi-phase microstructures can drastically alter the alloy's response. Given that both the Ga15 and Ga20 systems transition into a dual-phase (BCC + FCC) structure, further analysis is required to explain their enhanced performance during forward polarization. As established in the microstructural characterization section, these alloys consist of a Ga-Ni-rich BCC phase and a Cr-rich FCC phase.

It is well-established that chloride-containing environments are highly aggressive, as Cl^- ions preferentially target Cr-depleted phases. This localized attack disrupts the integrity of the Cr_2O_3-rich passive film, thereby facilitating the nucleation and propagation of pits and significantly compromising the alloy's overall corrosion resistance [31,34–36,57,59]. Since both the Ga15 and Ga20 alloys feature a dual-phase microstructure—with one phase being significantly depleted in Chromium—conventional metallurgical theory would predict a marked decline in their electrochemical stability. However, as demonstrated by the experimental data, these alloys do not exhibit the anticipated degradation in corrosion performance, suggesting a more complex protective mechanism at play.

Conversely, microstructural characterization revealed that the Gallium-bearing alloys exhibit a significantly more refined grain structure compared to the Ga0 baseline, with the Ga15 alloy displaying the highest degree of refinement. According to Shuang et al. [34], Fu et al. [58] and Olsson et al. [60], a reduction in grain size enhances corrosion resistance by downsizing potential galvanic couples to the microscale, thereby mitigating severe elemental segregation and promoting the formation of a more uniform, stable passive film. However, the categorical benefit of grain refinement remains a subject of debate in the literature. Wang et al. [29] suggested that an excessively fine grain structure may actually compromise corrosion resistance. This deterioration is attributed to the increased density of grain boundaries, which act as high-energy sites that facilitate accelerated metal ion dissolution and elevated reaction kinetics.

Furthermore, a high density of grain boundaries and dislocations can exacerbate localized galvanic corrosion by providing numerous active sites for dissolution. Conversely, in excessively coarse-grained structures, the relatively low grain boundary density retards the initial ion dissolution necessary to seed the passivating layer; this hinders the development of a continuous, stable passive film and subsequently reduces pitting resistance. Given these competing mechanisms, researchers have proposed that an intermediate grain size is optimal for maximizing corrosion resistance. For instance, in studies of single-phase CoCrFeNiMn HEAs, "fine" and "coarse" grain sizes were defined as 1.24 μm and 145.9 μm, respectively, with an optimal moderate size of 71.6 μm. In the present effort and by the application of the linear intersection method, it was found that the average grain size for the Ga20 alloy was 20 ± 4 μm and for the Ga15 system it was 12 ± 3 μm. The difference between the two systems is very small, especially as the mean values depict a very fine size. What is important to mention, nevertheless, is that in the case of the Ga15

alloy the Ga-rich phase it is considerably finer than that of the Ga20 phase as observed in Figure 2. Finally, it is essential to consider the thermodynamic perspective provided by Wang et al. [61], who noted that Cr_2O_3 oxides possess significantly higher thermodynamic stability and lower dissolution rates compared to the corresponding oxides of Fe and Ni.

The final consideration involves the specific role of Gallium within the alloy matrix. To the best of the authors' knowledge, the influence of Ga addition on the electrochemical corrosion response of the quintessential Cantor alloy (CoCrFeNiMn) has not yet been documented. However, studies by Gebert et al. [18], Wang et al. [44], Sanchez-Carrillo [17], and Amin et al. [36] on various Ni-Mn-Ga systems have identified a synergistic effect between Ga_2O_3 and NiO. This interaction appears to significantly enhance the nucleation, growth, and structural stability of the passive film. Other species, including $NiOH_2$, NiOOH, MnO_2 and MnO, likely contribute to the overall passivity of the system. Notably, none of these investigations reported the formation of Gallium hydroxides or oxyhydroxides, regardless of the electrolyte composition or the polarization parameters employed. This suggests that Gallium participates in the passivation process primarily through the formation of stable, anhydrous oxides.

By synthesizing the preceding observations, the following conclusions regarding the anodic forward scan of the CPP profiles—specifically the regions succeeding the activation-controlled Tafel domain—can be formulated:

(a) In the quaternary CoCrFeNi (Ga0) system, the onset of anodic polarization facilitates the formation of a passive film whose thermodynamic stability and protective capacity are predominantly attributed to the Cr_2O_3 oxide layer, with Co, Ni, and Fe contributing secondary stabilizing effects. As the polarization potential increases, the film composition evolves; according to Brito Garcia et al. [62], there is a progressive incorporation of hydroxide phases, such as $Ni(OH)_2$ and $Cr(OH)_3$. The protective efficacy of this passive film is eventually counterbalanced by the stochastic nucleation and propagation of pits, resulting in the observed monotonic increase in current density. Furthermore, the sustained electronic conductivity of the film at elevated overpotentials is influenced by the prevalence of hydroxides. As noted by Xing et al. [59], the lattice mismatch between the primary oxides and the secondary hydroxides induces a high density of dislocations. These structural irregularities generate acceptor energy levels within the band gap, thereby increasing the point defect density and charge carrier concentration, which manifests as significantly higher current densities.

(b) Regarding the Gallium-bearing alloys, Cl^- ions preferentially attack the Cr-depleted, Ni-Ga-rich BCC phase, initiating localized dissolution and acting as primary sites for pit nucleation and propagation. However, in these Chromium-deficient regions, Ni and Ga assume a dominant role in the passivation process. As the anodic potential increases, the formation of Ga_2O_3 alongside Ni, Co, and Fe oxides/hydroxides generates a secondary protective barrier. The CPP profiles indicate that this Ga-modified film exhibits a superior formation rate compared to the standard passive layer. Consequently, the dynamic equilibrium established between film growth on Cr-depleted zones, the sustained passivity of Cr-rich regions, and active pitting results in a net current density that is significantly lower than that of the quaternary Ga0 system.

(c) In a comparative analysis of the Ga15 and Ga20 alloys, the degree of microstructural refinement emerges as the governing factor in their electrochemical response. While both alloys follow an identical mechanistic sequence regarding passive film development and pitting nucleation, the coarser grain structure of the Ga20 system significantly alters the interfacial kinetics. Specifically, the reduced grain boundary density in the Ga20 alloy provides fewer active sites for the initial elemental dissolution required to seed the passivating layer. Furthermore, the coarser morphology

hinders the microscale distribution of interphase galvanic couples, resulting in a higher concentration of anodic current at specific sites and, consequently, more intensive pitting initiation and propagation. As demonstrated in the anodic forward scans of the corresponding CPP profiles, this manifested as higher current densities in the Ga20 system relative to the more refined Ga15 alloy.

Regarding the reverse polarization scan, the CPP profiles (Figure 5) indicate a consistent electrochemical trend across all examined systems. Specifically, every alloy exhibits a positive hysteresis loop, a diagnostic signature of localized pitting corrosion. As elucidated by Amin et al. [36] and Kaesche [63], this hysteretic behavior signifies that pit propagation persists during the reverse scan, driven by the autocatalytic nature of the pit chemistry, where localized acidification and chloride accumulation sustain dissolution. The presence of these positive loops, combined with the observation that the repassivation potential (E_{rp}) does not intersect the forward anodic branch at a potential significantly nobler than the initial $E_{corr,fwd}$, confirms that the initiated pits do not undergo repassivation. This indicates a high susceptibility to irreversible localized attack under the tested conditions.

Another important observation is that for all systems the cathodic current densities in the reverse scan are always higher than the corresponding ones at the forward scan. This is an indication of a reduction process in the remaining oxide film or in general in the passive film on the electrode surface [36]. What is even more crucial is the comparison between these reverse cathodic currents between the different systems. Observations from the cathodic regions of the CPP profiles indicate that the Ga0 alloy exhibits lower cathodic current densities compared to the Ga15 and Ga20 systems, the latter of which displays nearly identical current values. This divergence implies that the reductive dissolution of passive film products is more kinetically intensive in the Gallium-bearing alloys. Given that Cr_2O_3 is characterized by superior thermodynamic stability and the lowest dissolution rate among the constituent oxides [17,47], it can be inferred that the passive film integrity of the quaternary CoCrFeNi (Ga0) alloy remains superior to that of the Ga-modified systems at the conclusion of the reverse polarization scan. This finding is of critical importance, as the subsequent Electrochemical Impedance Spectroscopy (EIS) analysis—serving as the final stage of the electrochemical characterization—probes the interfacial properties and stability of the specimen surfaces in this precise terminal state.

4.4. Electrochemical Impedance Spectroscopy (EIS)

To streamline the analysis of the equivalent circuit elements, the following critical experimental conditions must be considered:

a. Surface state post-CPP: EIS measurements were conducted following the completion of the reverse polarization scan, specifically after the cathodic region where reductive dissolution of passive film products occurred.
b. Microstructural influence on pitting: While all systems exhibited pitting, the mechanisms differed by composition. In the single-phase Ga0 alloy, pitting initiated at the grain boundaries of the homogeneous FCC matrix. Conversely, in the dual-phase Ga15 and Ga20 alloys, pitting was localized within the Cr-depleted, Ni-Ga-rich BCC phase. This aligns with findings by Yamanaka et al. [30] and Shi et al. [31], who identify Cr-depleted regions as sensitized sites for preferential localized attack.

Consequently, a direct comparison across these disparate systems necessitates careful consideration. While the equivalent circuit parameters derived from Model C for the Ga15 and Ga20 systems are mutually comparable and reliable due to their shared dual-phase characteristics, benchmarking these results against the Model A parameters of the Ga0 system may lead to erroneous conclusions.

Regardless of the specific equivalent circuit model (EEC) employed, the electrode surface is conceptually bifurcated into two distinct electrochemical domains: the residual passive film persisting after Cyclic Potentiodynamic Polarization (CPP) and the active pitted regions established at the conclusion of the test. In both Models A and C, the intact passive film is represented by an ohmic resistance, R_{film}, in parallel with a Constant Phase Element, CPE_{film} (defined by the parameters Y_{film} and a_{film}). The pitted regions in Model A are characterized by a charge transfer resistance (R_{ct}) and a double-layer Constant Phase Element (CPE_{dl}), defined by Y_{dl} and a_{dl}. Conversely, Model C incorporates an additional time element, CPE_{diff} (defined by Y_{diff} and a_{diff} to account for the restricted diffusion kinetics observed within the localized environments of the Ga15 and Ga20 alloys).

The CPE_{film}/R_{film} network parameters provide critical insights into the physicochemical characteristics of the residual passive layer. According to Martin et al. [39], the concurrence of high R_{film}, low Y_{film}, and high a_{film} values signifies a highly condensed, structurally rigid, and protective film architecture. Conversely, a reduction in R_{film} accompanied by an increase in Y_{film} and a decline in a_{film} indicates a more defective, porous interface with diminished passivity. Within this framework, a comparison between the Gallium-bearing systems reveals relatively low R_{film} values for Ga15 and Ga20 (105.6 Ω and 134 Ω, respectively). However, the most salient divergence appears in the Constant Phase Element (CPE) parameters: Ga15 exhibits Y_{film} = 41.55 × 10^{-6} and a_{film} = 0.868, whereas Ga20 yields 54.22 × 10^{-6} and 0.802, respectively. These results clearly demonstrate that the Ga20 alloy possesses inferior protective capabilities compared to Ga15. Notably, the Ga0 system exhibited the most pronounced degradation (R_{film} = 79.95, Y_{film} = 80.59 × 10^{-6}, a_{film} = 0.785). It must be reiterated, however, that direct benchmarking between the Ga0 system and the Ga-alloyed variants is constrained by the distinct topological configurations of their respective equivalent electric circuits (EECs).

Beyond the physicochemical properties of the passive film, the CPE_{dl} and R_{ct} parameters exert a dominant influence on the overall corrosion resistance of the Ga0 system, a relationship elucidated in the subsequent sections. Nevertheless, the authors acknowledge that the definitive role of these interfacial kinetics requires further experimental validation. A notable point of concern is the significantly lower magnitude of R_{film} values obtained here compared to the established literature [30,31,34,35,39,40,46,48,49]. It is hypothesized that the cathodic currents encountered during the terminal stage of the reverse polarization scan facilitate the intensive destabilization and reductive dissolution of the passive layers. This process ostensibly enhances the surface conductivity of the exposed alloy matrix, thereby depressing the measured film resistance. Consistent with earlier assertions, further investigation is mandated to fully elucidate these mechanisms and reconcile the observed discrepancies.

A critical parameter in assessing electrochemical stability is the charge transfer resistance (R_{ct}) and its associated double-layer capacitance (CPE_{dl}). The magnitude of Y_{dl} and the exponent a_{dl} serve as indicators of surface heterogeneity, reflecting the compactness and structural integrity of the passive layer. Generally, a higher R_{ct} coupled with lower Y_{dl} and elevated a_{dl} values signifies superior corrosion resistance [22–25,30–33,36,39,56]. Analysis of the data in Table 3 reveals that the Ga0 alloy exhibits the highest R_{ct} among the tested systems, indicating a superior resistance to charge transfer across the interface. This observation aligns with the Cyclic Potentiodynamic Polarization (CPP) results (Figure 5); specifically, the Ga0 alloy displayed the lowest cathodic current densities at the termination of the reverse scan. This suggests a less extensive reductive dissolution of the residual passive film products, thereby confirming the superior electrochemical stability of the quaternary system in its terminal state.

A direct comparison of the Ydl of the Ga0 alloy with the Ydl of the Ga15 and the Ga20 alloy would be methodologically unsound. In the Ga15 and Ga20 alloys, the electrochemical response within the localized, porous pitted regions is governed by an additional time constant, CPE_{diff} (parameterized by Y_{diff}), which accounts for mass-transport limitations and diffusion kinetics absent in the Ga0 model. However, as the Ga15 and Ga20 alloys are modeled using an identical equivalent electrical circuit (EEC) topology, a comparative analysis between them is statistically and physically valid. The Ga15 alloy exhibits a lower Y_{dl} (34.32×10^{-6}) and a superior a_{dl} (0.829) relative to the Ga20 alloy (66.98×10^{-6} and 0.765, respectively). This divergence indicates that the Ga15 system possesses a more homogeneous and structurally intact interface within the active regions, further corroborating its enhanced resistance to localized degradation compared to the higher-Gallium-content variant.

Furthermore, a pronounced divergence in the diffusion-associated admittance (Y_{diff}) is observed between these two compositions. The Y_{diff} parameter quantifies the magnitude of the mass-transport impedance within the localized environment; specifically, lower Y_{diff} values correlate with reduced effective diffusion coefficients for metallic cations and oxygen species. This attenuation of ionic flux diminishes the overall reaction kinetics and, consequently, the corrosion current density (i_{corr}), thereby enhancing the electrochemical stability of the system [53]. This mechanistic relationship accurately characterizes the observed behavior of the Ga15 and Ga20 alloys, which yielded Y_{diff} values of 295.3×10^{-6} and 413.3×10^{-6}, respectively. This trend is remarkably consistent with the terminal cathodic current densities recorded during the reverse scan of the Cyclic Potentiodynamic Polarization (CPP) tests, reinforcing the evidence for superior transport-limited protection in the Ga15 system.

In summary, the preceding electrochemical characterization concludes that the quaternary Ga0 alloy exhibits the highest total polarization impedance (27.14 kΩ), followed by the Ga15 system (20.28 kΩ). The Ga20 alloy conversely displays the lowest impedance value (16.34 kΩ) indicating a relative decline in overall corrosion resistance as Gallium content increases beyond the 15% threshold.

5. Conclusions

- The CoCrFeNi base alloy was stabilized in a single-phase FCC solid solution.
- Ga additions led to the formation of a dual BCC-FCC microstructure.
- The BCC phase is rich in Ga and Ni.
- The relative fraction of the BCC phase increases with Ga addition (from 18–22% for the Ga15 to 31–34% for the Ga20 respectively).
- EFM tests revealed that Ga addition reduces the corrosion response (Icorr: 4.142, 5.619 and 10.01 μA/cm2, and Rp: 12,035, 10,736 and 7254 ohms for the Ga0, Ga15 and Ga20 alloys respectively).
- CPP diagrams showed positive hysteresis loops and a lack of repassivation, indicating a high susceptibility to stable pit growth upon the breakdown of the passive film,
- The EIS analysis confirmed that while Ga-doped alloys exhibit an increase in passive film resistance (Rfilm: 79.95, 105.6 and 134 ohms for Ga0, Ga15 and Ga20 alloys respectively), this is offset by a sharp decline in charge transfer resistance (Rct: 22,620, 11,380, 10,060 ohms for Ga0, Ga15 and Ga20 alloys respectively).
- The combination of EFM, CPP and EIS can provide a holistic approach in assessing the electrochemical corrosion response of various conventional and high-entropy alloy systems.

Author Contributions: Conceptualization, E.G. and A.E.K.; methodology, E.G., A.E.K. and T.E.M.; formal analysis, E.G., A.E.K., S.K., A.L., C.P. and M.Z.; investigation, S.K., A.L., C.P., M.Z. and T.E.M.; writing—original draft preparation, A.P. and A.E.K.; writing—review and editing, A.P. and A.E.K.; visualization, E.G., A.E.K. and T.E.M.; supervision, T.E.M. and A.E.K. All authors have read and agreed to the published version of the manuscript.

Funding: This research received no external funding.

Data Availability Statement: The original contributions presented in this study are included in the article. Further inquiries can be directed to the corresponding author.

Conflicts of Interest: The authors declare no conflicts of interest.

References

1. Yeh, J.W.; Chen, S.K.; Lin, S.J.; Gan, J.Y.; Chin, T.S.; Shun, T.T.; Tsau, C.H.; Chang, S.Y. Nanostructured High-Entropy Alloys with Multiple Principal Elements: Novel Alloy Design Concepts and Outcomes. *Adv. Eng. Mater.* **2004**, *6*, 299–303. [CrossRef]
2. Cantor, B.; Chang, I.T.H.; Knight, P.; Vincent, A.J.B. Microstructural Development in Equiatomic Multicomponent Alloys. *Mater. Sci. Eng. A* **2004**, *375–377*, 213–218. [CrossRef]
3. Cantor, B. The Thermodynamics of Multicomponent High-Entropy Materials. *J. Mater. Sci.* **2025**, *60*, 1750–1764. [CrossRef]
4. Yamg, H.; Shang, X.; Wang, L.; Wang, Z.; Wang, J.; Lin, X. Effect of Constituent Elements on the Corrosion Resistance of Single-Phase CoCrFeNi High-Entropy Alloys in NaCl Solution. *Acta Metall. Sin.* **2018**, *54*, 905–910.
5. Li, J.; Yamanaka, K.; Chiba, A. Significant Lattice-Distortion Effect on Compressive Deformation in Mo-added CoCrFeNi-based High-Entropy Alloys. *Mater. Sci. Eng. A* **2022**, *830*, 142295. [CrossRef]
6. Guo, S.; Ng, C.; Lu, J.; Liu, C.T. Effect of Valence Electron Concentration on Stability of Fcc or Bcc Phase in High Entropy Alloys. *J. Appl. Phys.* **2011**, *109*, 103505. [CrossRef]
7. Liu, X.; Sun, M.; Fang, Q.; Meng, X.; Liang, L. Effect of Ga addition on the damping and mechanical properties of FeCoCrNi high entropy alloys. *J. Alloys Compd.* **2026**, *1051*, 185963. [CrossRef]
8. Vida, A.; Maksa, Z.; Molnar, D.; Huang, S.; Kovac, J.; Varga, L.K.; Vitos, L.; Chinh, N.Q. Evolution of the Phase Structure after Different Heat Treatments in NiCoFeCrGa High Entropy Alloy. *J. Alloys Compd.* **2018**, *743*, 234–239. [CrossRef]
9. Molnar, D.; Vida, A.; Huang, S.; Chinh, N.Q. The Effect of Cooling Rate on the Microstructure and Mechanical Properties of NiCoFeCrGa High-Entropy Alloy. *J. Mater. Sci.* **2019**, *54*, 5074–5082. [CrossRef]
10. Luo, Z.; Zhou, X.-P. Liquid-metal-mediated low-temperature sintering synthesis of high-entropy alloys with on-demand composition and performance. *Cell Rep. Phys. Sci.* **2025**, *6*, 103022. [CrossRef]
11. Wang, J.; Yang, S.; Lin, Y.; Shu, D.; Wang, S. Mechanical properties and biological performance of Ga-containing TiZrNb medium-entropy alloy for biomedical implants. *J. Alloys Compd.* **2025**, *1026*, 180364. [CrossRef]
12. Zhu, X.; Wang, J.; Du, Y.; Zhang, J.; Wan, S.; Shub, D.; Liu, Y.; Li, F.; Lin, Y.; Yang, Y.; et al. Gallium containing high entropy alloy inhibits biofilm formation and enhances osseointegration. *Compos. Part B* **2025**, *295*, 112194. [CrossRef]
13. Song, G.; Fu, D.; Lin, Y. Corrosion Resistance Prediction of High-Entropy Alloys: Framework and Knowledge Graph-Driven Method Integrating Composition, Processing, and Crystal Structure. *npj Mater. Degrad.* **2025**, *9*, 81. [CrossRef]
14. Obot, I.B.; Onyeachu, B. Electrochemical Frequency Modulation (EFM) Technique: Theory and Recent Practical Applications in Corrosion Research. *J. Mol. Liq.* **2018**, *249*, 83–96. [CrossRef]
15. Esmailzadeh, S.; Aliofkhazraei, M.; Sarlak, H. Interpretation of Cyclic Potentiodynamic Polarization Test Results for Study of Corrosion Behavior of Metals: A Review. *Prot. Met. Phys. Chem. Surf.* **2018**, *54*, 976–989. [CrossRef]
16. Sáez-Pardo, F.; Giner-Sanz, J.J.; Pérez-Herranz, V. Equivalent Electrical Circuit recommendation for Electrochemical Impedance Spectroscopy: A benchmark of different Machine Learning algorithms. *J. Electroanal. Chem.* **2025**, *976*, 118812. [CrossRef]
17. Sanchez-Carrillo, M.; Flores de los Rios, J.P.; Huape-Padilla, E.; Bautista Margulis, R.G.; Flores-Zuñiga, H.; Ferrer-Sanchez, M.I.; López-Ocaña, G.; Chacón-Nava, J.G.; Martinez-Villafañe, A. Electrochemical and Mechanical Behavior in Polycrystalline Co-Ni-Ga Shape Memory Alloys. *Int. J. Electrochem. Sci.* **2014**, *9*, 7725–7735. [CrossRef]
18. Gebert, A.; Roth, S.; Oswald, S.; Schultz, L. Passivity of Polycrystalline NiMnGa Alloys for Magnetic Shape Memory Applications. *Corr. Sci.* **2009**, *51*, 1163–1171. [CrossRef]
19. Bosch, R.W.; Hubrecht, J.; Bogaerts, W.F.; Syrett, B.C. Electrochemical Frequency Modulation: A New Electrochemical Technique for Online Corrosion Monitoring. *Corrosion* **2001**, *57*, 60–70. [CrossRef]
20. Dévay, J.; Mészáros, L. Study of the Rate of Corrosion of Metals by a Faradaic Distortion. *Acta Chim. Acad. Sci. Hung.* **1979**, *100*, 183.
21. Mészáros, L.; Mészáros, G.; Lengyel, B. Application of Harmonic Analysis in the Measuring Technique of Corrosion. *J. Electrochem. Soc.* **1994**, *141*, 2068. [CrossRef]

22. Gill, J.S.; Allow, M.; Scantlebury, J.D. Corrosion Measurements Derived from Small Perturbation Non-Linearity—Part 1: Harmonic Analysis. *Corrosion* **1983**, *39*, 61–66. [CrossRef]
23. Sathiyanarayanan, S.; Balakrishnan, K. Critique of Harmonic Analysis for Corrosion Rate Measurements. *Corros. Eng. Sci. Technol.* **1994**, *29*, 152. [CrossRef]
24. Pirnát, A.; Mészáros, L.; Lengyel, B. A Comparison of Electrochemical and Analytical Chemical Methods for the Determination of the Corrosion Rate with very Efficient Inhibitors. *Corros. Sci.* **1995**, *37*, 963. [CrossRef]
25. McKubre, M.C.H.; Syrett, B.C. ASTM STP908, Harmonic Impedance Spectroscopy for the Determination of Corrosion Rates in Cathodically Protected Systems. In *Corrosion Monitoring in Industrial Plants Using Nondestructive Testing and Electrochemical Methods*; Moran, G.C., Labine, P., Eds.; ASTM: West Conshohocken, PA, USA, 1986; Volume 433.
26. Macdonald, J.R. *Impedance Spectroscopy Emphasizing Solid Materials and Systems*; John Wiley and Sons: New York, NY, USA, 1987; Volume 267.
27. Kus, E.; Mansfeld, F. An Evaluation of the Electrochemical Frequency Modulation (EFM) Technique. *Corr. Sci.* **2006**, *48*, 965–979. [CrossRef]
28. Stern, M.; Geary, A.L. Electrochemical Polarization I. A Theoretical Analysis of the Shape of Polarization Curves. *J. Electrochem. Soc.* **1957**, *104*, 56–63. [CrossRef]
29. Wang, Y.; Jin, J.; Zhang, M.; Wang, X.; Gong, P.; Zhang, J.; Liu, J. Effect of the Grain Size on the Corrosion Behavior of CoCrFeMnNi HEAs in a 0.5 M H_2SO_4 Solution. *J. Alloys Compd.* **2021**, *858*, 157712. [CrossRef]
30. Yamanaka, K.; Shiratori, H.; Mori, M.; Omura, K.; Fujieda, T.; Kuwabara, K.; Chiba, A. Corrosion Mechanism of an Equimolar AlCoCrFeNi High-Entropy Alloy Additively manufactured by electron beam melting. *npj Mater. Degrad.* **2020**, *4*, 24. [CrossRef]
31. Shi, Y.; Yang, B.; Xie, X.; Brechtl, J.; Dahmen, K.A.; Liaw, P.K. Corrosion of Al_xCoCrFeNi High-Entropy Alloys: Al-content and Potential Scan-rate Dependent Pitting Behavior. *Corr. Sci.* **2017**, *119*, 33–45. [CrossRef]
32. Patel, K.; Sadeghilaridjani, M.; Pole, M.; Mukherjee, S. Hot Corrosion Behavior of Refractory High Entropy Alloys in Molten Chloride Salt for Concentrating Solar Power Systems. *Sol. Energy Mater. Sol. Cells* **2021**, *230*, 111222. [CrossRef]
33. Zhu, Y.; Liu, Y.; Meng, Z.; Tian, J. Microstructure, Mechanical Properties, and Electrochemical Corrosion Behavior of CoCrFeNiNb and CoCrFeNiV High-Entropy Alloys Prepared via Mechanical Alloying and Spark Plasma Sintering. *Metals* **2025**, *15*, 814. [CrossRef]
34. Shuang, S.; Ding, Z.Y.; Chung, D.; Shi, S.Q.; Yang, Y. Corrosion Resistant Nanostructured Eutectic High Entropy Alloy. *Corr. Sci.* **2020**, *164*, 108315. [CrossRef]
35. Xu, K.X.; Zhu, M.; Yuan, Y.F.; Guo, S.Y. Research on Electrochemical Corrosion and Passive Behavior of CoCrFeNi High-Entropy Alloy Compared with 304 Stainless Steel in a NaCl Environment. *J. Mater. Eng. Perform.* **2024**, *34*, 3755–3766. [CrossRef]
36. Amin, M.A.; El-Bagoury, N.; Shokry, H. Corrosion and Electrochemical Behavior of Ni51Fe22-xGa27Tix Magnetic Shape Memory Alloys in 0.1 M NaCl Solution at Different Temperatures. *Int. J. Electrochem. Sci.* **2013**, *8*, 2791–2805. [CrossRef]
37. Mc Cafferty, E. Validation of Corrosion Rates Measured by the Tafel Extrapolation Method. *Corr. Sci.* **2005**, *47*, 3202–3215. [CrossRef]
38. Burstein, G. A Hundred Years of Tafel Equation: 1905–2025. *Corr. Sci.* **2005**, *47*, 2858–2870. [CrossRef]
39. Martin, U.; Ress, J.; Pérez, P.; Adeva, P.; Bastidas, D.M. Corrosion Behavior of $Al_{10}Cr_{30}Fe_{25}Mn_{30}Ti_5$ High-Entropy Alloy: Microstructural, Electrochemical, and Surface Analysis. *Metals* **2022**, *12*, 1736. [CrossRef]
40. Fang, S.; Chen, K.; Yao, H.; Cao, Y.; Guo, S.; Wang, L.; Wang, Y.; Yu, S.; Wang, N. Preparation of Gallic Acid Intercalated Layered Double Hydroxide for Enhanced Corrosion Protection of Epoxy Coatings. *Coatings* **2023**, *13*, 128. [CrossRef]
41. Yan, D.; Song, K.; Sun, H.; Wu, S.; Zhao, K.; Zhang, H.; Yuan, S.; Kim, J.T.; Chawake, N.; Ren, O.; et al. Microstructures, Mechanical Properties, and Corrosion Behaviors of Refractory High-Entropy ReTaWNbMo Alloy. *J. Mater. Eng. Perform.* **2020**, *29*, 399–409. [CrossRef]
42. Feliu, S., Jr. Electrochemical Impedance Spectroscopy for the Measurement of the Corrosion Rate of Magnesium Alloys: Brief Review and Challenges. *Metals* **2020**, *10*, 775. [CrossRef]
43. Patel, K.; Mahajan, C.; Muskeri, S.; Mukherjee, S. Corrosion Behavior of Refractory High-Entropy Alloys in FLiNaK Molten Salts. *Metals* **2023**, *13*, 450. [CrossRef]
44. Wang, Y.; Cheng, H.; Zhang, X.; Doing, Z. Effect of Ni on the Corrosion Resistance and Passivation Characteristics of Ni-Mn-Ga-Gd Shape Memory Alloys in Sodium Chloride Solutions. *Appl. Surf. Sci.* **2025**, *680*, 161395. [CrossRef]
45. Wang, Q. Electrochemical Evaluation of Nanostructured Coatings for Corrosion Protection of Structural Metals. *Int. J. Electrochem. Sci.* **2025**, *20*, 101214. [CrossRef]
46. Boldrini Nascimento, C.; Donatus, U.; Triveño Ríos, C.; Altobelli Antunesa, R. Electronic Properties of the Passive Films Formed on CoCrFeNi and CoCrFeNiAl High Entropy Alloys in Sodium Chloride Solution. *J. Materres. Technol.* **2020**, *9*, 13879–13892.
47. Boldrini Nascimento, C.; Donatus, U.; Triveño Ríos, C.; Lopes de Oliveira, M.C.; Altobelli Antunes, R. A Review on Corrosion of High Entropy Alloys: Exploring the Interplay Between Corrosion Properties, Alloy Composition, Passive Film Stability and Materials Selection. *Mater. Res.* **2022**, *25*, 20210442. [CrossRef]

48. Cabrera-Peña, J.; Brito-Garcia, S.J.; Mirza-Rosca, J.C.; Callico, G.M. Electrical Equivalent Circuit Model Prediction of High-Entropy Alloy Behavior in Aggressive Media. *Metals* **2023**, *13*, 1204. [CrossRef]
49. Orozco-Cruz, R.; Galván-Martínez, R.; Martinez, E.A.; Fernández-Gómez, I. Electrochemical Impedance Spectroscopy (EIS) Applied to Study to Aluminium Alloys Degradation in Saline Solution. *ECS Trans.* **2010**, *29*, 73–80. [CrossRef]
50. Luo, H.; Li, Z.; Mingers, A.M.; Raabe, D. Corrosion Behavior of an Equiatomic CoCrFeMnNi High-Entropy Alloy Compared with 304 Stainless Steel in Sulfuric Acid Solution. *Corr. Sci.* **2018**, *134*, 131–139. [CrossRef]
51. Hermas, A.A.; Morad, M.S. A Comparative Study on the Corrosion Behaviour of 304 Austenitic Stainless Steel in Sulfamic and Sulfuric Acid Solutions. *Corr. Sci.* **2008**, *50*, 2710–2717. [CrossRef]
52. Lazanas, A.C.; Prodromidis, M.I. Electrochemical Impedance Spectroscopy A Tutorial. *ACS Meas. Sci.* **2023**, *3*, 162−193. [CrossRef]
53. Harrington, D.; van den Driessche, P. Mechanism and Equivalent Circuits in Electrochemical Impedance Spectroscopy. *Electrochim. Acta* **2011**, *56*, 8005–8013. [CrossRef]
54. Abdel-Rehim, S.S.; Khaleda, K.S.; Abd-Elshafi, N.S. Electrochemical Frequency Modulation as a New Technique for Monitoring Corrosion Inhibition of Iron in Acid Media by New Thiourea Derivative. *Electrochim. Acta* **2006**, *51*, 3269–3277. [CrossRef]
55. Khaled, K.F. Application of Electrochemical Frequency Modulation for Monitoring Corrosion and Corrosion Inhibition of Iron by Some Indole Derivatives in Molar Hydrochloric Acid. *Mater. Chem. Phys.* **2008**, *112*, 290–300. [CrossRef]
56. Megremis, S.J. Corrosion Resistance of Precious Metals for Biomedical Applications. In *Precious Metals for Biomedical Applications*; Woodhead Publishing Series in Biomaterials: Number 77; Baltzer, N., Copponnex, T., Eds.; Elsevier: Amsterdam, The Netherlands, 2014; Chapter 3; pp. 56–86.
57. Alshamsi, A.S.; Alkaabi, A.Y.; AlBlooshi, A.G. Influence of Chloride Ion Concentration on the Corrosion Behavior of 304 Austenitic Stainless Steel in Sulfuric Acid. *Int. J. Electrochem. Sci.* **2026**, *21*, 101257. [CrossRef]
58. Fu, Y.; Li, J.; Luo, H.; Du, C.; Li, C. Recent Advances on Environmental Corrosion Behavior and Mechanism of High-Entropy Alloys. *J. Mater. Sci. Technol.* **2021**, *80*, 217–233. [CrossRef]
59. Xing, B.; Jin, B.; Zhan, X.; Xu, X.; Zhang, N.; Zuo, X. Effects of Polarization Potential on the Passive Film Properties of CoCrFeNi High-Entropy Alloy. *J. Alloy Compd.* **2025**, *1032*, 181061. [CrossRef]
60. Olsson, C.O.A.; Landolt, D. Passive Films on Stainless Steels-Chemistry, Structure and Growth. *Electrochem. Acta* **2003**, *48*, 1093–1104. [CrossRef]
61. Wang, L.; Mercier, D.; Zanna, S.; Seyeux, A.; Laurent-Brocq, M. Study of the Surface Oxides and Corrosion Behavior of an Equiatomic CoCrFeMnNi High Entropy Alloy by XPS and TOF-SIMS. *Corros. Sci.* **2020**, *167*, 108507. [CrossRef]
62. Brito-Garcia, S.J.; Mirza-Rosca, J.C.; Jimenez-Marcos, C.; Voiculescu, I. EIS Study of Doped High-Entropy Alloy. *Metals* **2023**, *13*, 883. [CrossRef]
63. Kaesche, H. Microtunnelling during Selective Alloy Dissolution and during Pitting. *Werkst. Korros.* **1988**, *39*, 152–161. [CrossRef]

Disclaimer/Publisher's Note: The statements, opinions and data contained in all publications are solely those of the individual author(s) and contributor(s) and not of MDPI and/or the editor(s). MDPI and/or the editor(s) disclaim responsibility for any injury to people or property resulting from any ideas, methods, instructions or products referred to in the content.